Materials & Design 225 (2023) 111535

Contents lists available at ScienceDirect

Materials & Design

journal homepage: www.elsevier.com/locate/matdes

Influence of the deposition process and substrate on microstructure, phase composition, and residual stress state on as-deposited Cr-Al-C coatings

Stefan Heinze [a,*], Tim Krülle [a,b], Lars Ewenz [a,b], Christina Krywka [c], Anton Davydok [c], Andreas Stark [d], Rainer Cremer [e], Christoph Leyens [a,b]

[a] Technische Universität Dresden, Institute of Materials Science IfWW, Helmholtzstr. 7, 01069 Dresden, Germany
[b] Fraunhofer Institute for Material and Beam Technology IWS, Winterbergstr. 28, 01277 Dresden, Germany
[c] Helmholtz-Zentrum Hereon, Institute of Materials Physics, Notkestr. 85, 22607 Hamburg, Germany
[d] Helmholtz-Zentrum Hereon, Institute of Materials Physics, Max-Planck-Str.1, 21502 Geesthacht, Germany
[e] KCS Europe GmbH, Am Handwerkerzentrum 6, 52156 Monschau, Germany

HIGHLIGHTS

- The thin films consist of amorphous and metastable $(Cr,Al)_2C$, with the ratio dependent on the coating process and substrate.
- Residual stress analysis was performed with in situ and ex-situ synchrotron X-ray diffraction.
- Amorphous volumes, with a higher connection area to the substrate, mainly buffer the residual stress from the deposition.
- Compressive residual stress reduces tensile stress caused by cooling, but is not stable during post-heat treatment at 700 °C.

GRAPHICAL ABSTRACT

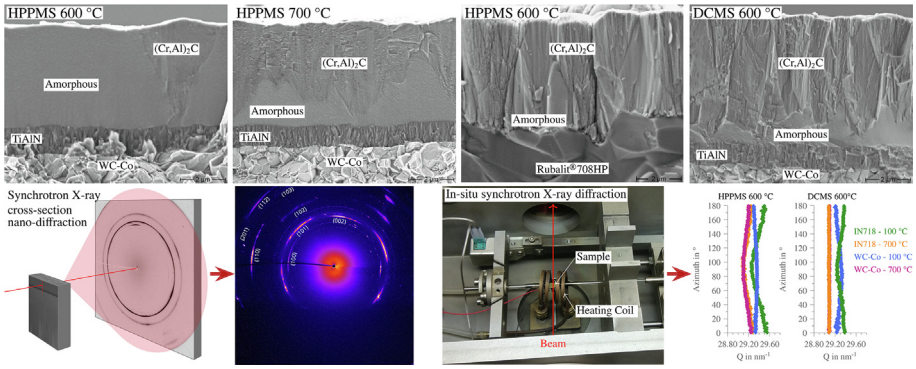

ARTICLE INFO

Article history:
Received 3 July 2022
Revised 6 December 2022
Accepted 22 December 2022
Available online 24 December 2022

Keywords:
Cr_2AlC MAX phase
Metastable $(Cr,Al)_2C$
Amorphous Cr-Al-C
Thin films
Residual Stress
Synchrotron X-ray diffraction

ABSTRACT

This paper focuses on the influence of the High Power Pulsed Magnetron Sputtering (HPPMS) and Direct Current Magnetron Sputtering (DCMS) coating deposition processes, the bias voltage, deposition temperature, and substrate on various properties of the as-deposited state of Cr-Al-C thin films. Three substrates with different coefficients of thermal expansion and electrical conductivity were used. To investigate the microstructure, phase composition, residual stress state, and mechanical properties, ex-situ and in situ synchrotron experiments were conducted accompanied by electron microscopy and nanoindentation. As-deposited Cr-Al-C coatings consisted of amorphous and crystalline areas, with the ratio highly dependent on the deposition process and substrate. The crystalline phase was identified as metastable $(Cr,Al)_2C$. The highest crystallinity was determined for DCMS coatings. Increasing temperature and decreasing bias voltage increased coating crystallinity for HPPMS coatings. The influence of the deposition process and bias voltage was highly reduced for the substrate with low electrical conductivity. In-situ investigations of the stress state of amorphous areas revealed, that those were acting as a residual stress buffer. The

* Corresponding author.
E-mail addresses: stefan.heinze@tu-dresden.de (S. Heinze), tim.kruelle@tu-dresden.de (T. Krülle), lars.ewenz@iws.fraunhofer.de (L. Ewenz), christina.krywka@hereon.de (C. Krywka), anton.davydok@hereon.de (A. Davydok), andreas.stark@hereon.de (A. Stark), cremer@kcs-europe.de (R. Cremer), christoph.leyens@iws.fraunhofer.de, christoph.leyens@tu-dresden.de (C. Leyens).

https://doi.org/10.1016/j.matdes.2022.111535

hardness and Young's modulus of the coatings were found to increase with crystallinity and were slightly increased for crystalline HPPMS coatings compared to DCMS coatings.

1. Introduction

MAX or $M_{n+1}AX_n$ phases – M stands for transition metal, A for A-Group element, and X for C or N – are characterized by a hexagonal structure, where the M, A, and C layers are arranged in alternating order along the c-axis. This structure results in a covalent/ionic bond between the M and X elements, whereas the bond between M and A elements is metallic [1]. The different bonding characteristics yield a unique combination of properties such as high hardness and Young's modulus, oxidation and corrosion resistance combined with thermal shock resistance, and good thermal and electric conductivity [1–4].

Cr_2AlC, as a representative of the class of MAX phases, outstands other phases of this material class due to the oxidation resistance in air, turbine environments, and primary water. This resistance stems from the selective Al-oxidation and formation of a protective alumina scale in the case of the first two and a thin chromium oxide layer in the case of the last-mentioned environment [1,5–8]. Thus, Cr_2AlC is a promising material for protective coatings in high-temperature environments like turbine engines as well as materials for accident tolerant fuel cladding [6,8,9].

For Cr_2AlC thin-film synthesis, usually, Physical Vapor Deposition (PVD) techniques like Direct Current Magnetron Sputtering (DCMS) and High Power Pulsed Magnetron Sputtering (HPPMS) are used [10,11]. For the sputtering processes elemental [10,12] and composite [13,14] targets are common. In addition, successful Cr_2AlC coating deposition was achieved by Arc-PVD [15], low-energy pulsed electrospark deposition (PED) [16] as well as different sputtering routes by using a multilayer approach with elemental layers in combination with an annealing post-treatment [17].

PVD processes are often unique for the wide range of possible coating properties, due to different phase compositions and microstructures, stemming from the variety of possible energy – mainly the thermal energy at the substrate surface and kinetic energy of the sputtered flux – during the process. Using DCMS, a broader columnar microstructure can be achieved, while HPPMS is known for very dense coatings with fine microstructure and the possibility of inhibiting the columnar growth, due to the several orders of magnitudes higher target power density and the associated higher ionization rate of the sputtered species [18]. In combination with the Bias voltage, hence the increased bombardment of the growing coating, the atom mobility on the coating surface is increased [18].

Besides the possibility of a tailored microstructure, a few studies investigated the influence of the deposition process and the deposition parameters – mainly Bias voltage, substrate temperature, and target power density – on the elemental composition, phase composition, and microstructure of Cr_2AlC coatings. Mertens et al. [10] determined the elemental composition ranges for single-phase Cr_2AlC coatings to be $1.42 < Cr/Al < 2.03$ and $1.72 < Cr/C < 1.93$. Outside of these composition ranges, Cr_7C_3, $Cr_{23}C_6$, and Cr_2-Al impurities are often present in the deposited coatings [10,19]. The influence of the Bias voltage and peak power density – the comparison between DCMS and HPPMS – on the composition of Cr-Al-C coatings was investigated by Rueß et al. [20]. They found, that mainly Al is affected as a result of re- and self-sputtering through the high kinetic energy of the sputtered flux and determined Al deficiencies up to 20.4 at.% for the HPPMS process and Bias of −400 V [20].

Another important topic of various studies to date is the possible metastable and stable Cr_2AlC phases. The lowest substrate temperature for the existence of Cr_2AlC is reported for the DCMS process to be 300 °C, for a Ti-Cr-Al-C coating, and 450 °C for Cr-Al-C coatings [13,19]. Below 300°C only amorphous coatings were deposited [9,19,13]. Shtansky et al. [19] first described a metastable $(Cr,Al)_2C$ phase, a solid solution of Al in hexagonal Cr_2C (space group $P6_3/mmc$, prototype Mo_2C [21]), present in Cr-Al-C coatings deposited at 300 °C substrate temperature. Another metastable $(Cr,Al)_2C_x$ phase, with a similar space group and prototype as $(Cr,Al)_2C$, was proposed by Adulkadhim et al. [22], as the intermediate phase of the Cr_2AlC phase formation during the annealing post-treatment of amorphous Cr-Al-C coatings. Both phases show a decreased lattice parameter c in the range of 1/3 of c_{Cr_2AlC}. During the last years, mainly $(Cr,Al)_2C_x$ was used to describe the metastable state of Cr_2AlC coatings in the as-deposited state and as an intermediate phase of the Cr_2AlC formation process. However, because both metastable phases have a similar crystal structure, they share the same diffraction peaks – with slightly different positions due to different published lattice parameters – and no distinct differences are published up to the present [19,22].

A disordered Cr_2AlC phase with a decreased a (a_{Cr_2AlC}=2.863 Å to $a_{dis.\,Cr_2AlC}$=2.772 Å) and increased c (c_{Cr_2AlC}= 12.82 Å to $c_{dis.\,Cr_2AlC}$=13.26 Å) lattice parameter – attributed to the partial disordering of metal atoms in Cr_2AlC – was described by Zamulaeva et al. [16] for Cr_2AlC formation via pulsed electrospark deposition but is not yet considered as an intermediate or metastable phase for Cr_2AlC phase formation.

Recently, Rueß et al. [23] investigated the effect of the kinetic energy of the sputtered flux on the Cr_2AlC phase formation and found that the formation of the metastable phase is favored for high Bias voltage and target peak power densities. This is attributed to the detrimental effect of a too high kinetic energy of the sputtered flux, thus the energetic atom and ion bombardment hinder the growth of the large Cr_2AlC unit cell [23,24].

For thin-film applications under thermal load, the coating-substrate combination is a crucial factor for coating and thereby component lifetime. If the coefficient of thermal expansion (CTE) between the coating and the substrate is different to a certain extent, residual stresses will arise during heating and cooling and may cause coating failure. As described in [6], Cr_2AlC's inherent high CTE makes these coatings in particular suitable for metallic substrates like Ni-base superalloys. However, in combination with substrates with a low CTE like WC–Co or ceramic substrates, which are used in this study, coating failure is possible [6].

During the past years, a wide range of different deposition parameters was used for the deposition of amorphous Cr-Al-C, metastable, and Cr_2AlC coatings. Bias voltage ranging from floating potential to −400 V, substrate temperatures ranging from not actively heated to 850 °C, different target power densities, substrate-target distances, and other parameters, influence the thermal and kinetic energy of the deposition process and whereby affecting the resulting coating properties, in combination with different substrates, were used [10,11,13,19,23,25]. However, the influence of the substrate on the coating properties, with the consideration of a possibly reduced effect of the higher ionization rate of the HPPMS process and Bias voltage for substrates with high electrical resistivity, is not investigated in detail. Additionally, the influence of substrates with a distinct CTE misfit to Cr_2AlC, which

can cause severe residual stress during cooling from deposition temperature and the effect of the ion bombardment during deposition on the residual stress state is not yet investigated in detail. Both topics need to be addressed in order to fabricate protective Cr_2AlC coatings.

This is where this article aims to contribute. Cr-Al-C coatings were deposited using the HPPMS and DCMS deposition process, with the variation of the Bias voltage and deposition temperature to produce coatings with a wide property range on different substrates with high and low electrical resistivity and CTE. The microstructure, elemental and phase composition, mechanical properties as well as a qualitative analysis of the residual stress is provided for the as-deposited state. In addition, emphasis is on the discussion of the mechanisms behind the different influences on the coating properties. The investigations in this paper are continued in a second paper [26], which investigates the influence of the as-deposited state on the Cr_2AlC phase formation during heat treatment of a selection of the coating-substrate combination discussed in this paper.

2. Materials and methods

2.1. Coating deposition

In order to investigate the effect of the deposition process and parameters on the as-deposited state of Cr-Al-C coatings, deposition of thin Cr-Al-C films was performed with HPPMS and DCMS with a variation in deposition temperature and bias voltage. A summary of the main deposition parameters is given in Table 1. To produce a high number of samples without distinct positioning effects – composition variations or variance in grain orientation – and batch dependency, the HPPMS and DCMS depositions were carried out in the industrial-sized coater Kobelco S40 by KCS Europe GmbH. Samples were positioned on a rotating holder (ø=600 mm) in the center of the coater. Two Cr-Al-C composite targets from Plansee AG with a width of 80 mm and height of 505 mm – located around the holder and arranged opposite each other – were used. The heaters in the chamber were located between the targets. Before deposition, the chamber was heated to the respective temperature (chamber temperature in Table 1) and controlled by one thermal couple in the vicinity of the samples and one located near the heaters. During deposition, the chamber temperature was controlled by the thermal couple in the vicinity of the heaters. Therefore, the stated temperatures in Table 1 correspond to chamber temperature outside the plasma and the resulting peak temperature of the samples in the plasma during deposition was higher due to the influence of ion bombardment in dependence on the bias voltage (see Section 3.1). However, because the used coater was built for contract deposition, additional analysis periphery – for the measurement of the target current density, plasma analysis and monitoring the sample temperature during deposition – was not available.

As a result of planetary rotation during deposition, the samples were only approx. 2.5 s in the plasma for one revolution, equals 8 % during the whole deposition. Because the targets were located at 0° and 180°, samples were heated cyclically for approx. 1.3 s and cooled for 13.7 s during a half revolution.

In order to investigate the influence of the substrate on the as-deposited state of Cr-Al-C coatings, Inconel 718 (IN718) – a Ni-based superalloy as a representative for high CTE and high electrical conductivity [27] –, tungsten carbide-cobalt (WC–Co) of grade K40UF with 10 wt.% Co and 0.6 µm WC grain size – a representative for low CTE and high electrical conductivity –, and Rubalit®708HP – an alumina-based material as a representative for low CTE and high electric resistivity [28] – were used.

Investigations regarding residual stress and phase formation were performed at temperatures up to 900 °C. To prevent interdiffusion between the substrate and the Cr-Al-C coatings, a 1 µm TiAlN interdiffusion barrier – 29 at.% Ti, 25 at.% Al and 46 at.% N – was applied for IN718 and WC–Co samples. The TiAlN coatings were deposited in the Kobelco S40 coater using Arc-PVD with a substrate temperature of 600 °C and −50 V bias.

The electrical resistivity and the CTE of the substrates and interdiffusion barrier are summarized in Table 2. The terms WC–Co and IN718 in the following always refer to the respective substrate with the TiAlN interdiffusion barrier.

2.2. Coatings characterization

2.2.1. Electron microscopy for microstructure and elemental composition analysis

For the microstructure and film thickness investigation of the as-deposited films, the WC–Co and Rubalit®708HP samples were used for cryo-crack cross-section preparation. The cross-section preparation via grinding and polishing of the tempered samples was performed on the IN718 samples because the lower hardness compared to WC–Co led to an improved surface of the cross-section. The imaging was performed with the scanning electron microscope (SEM) Zeiss DSM 982 Gemini with a field emission gun using a combined mode of a secondary electron detector and an Everhart–Thornley detector, with an acceleration voltage of 5 kV.

The elemental composition was determined by energy dispersive X-ray spectroscopy (EDS) using a JEOL JSM-7800F field emission SEM with an EDS detector from Oxford Instruments, and an acceleration voltage of 10 kV.

2.2.2. Synchrotron X-ray diffraction analysis

The coatings phase composition and texture were determined by X-ray cross-section nano-diffraction analysis at the P03 Nanofokus End-Station of the light source PETRA III at DESY, Hamburg [34] – henceforth referred to as P03 experiment.

Samples were sliced into 200 µm thin 10 mm long bars with a height of 1 mm, followed by the removal of approx. 20 µm ×

Table 1
Overview of deposition parameters for used coatings. For confidentiality reasons, the complete set of parameters cannot be given and some parameters are only available as ranges.

Coating	HPPMS-600	HPPMS-600/-70 V	HPPMS-700	DCMS-600
Deposition process	HPPMS	HPPMS	HPPMS	DCMS
Chamber temperature	600 °C	600 °C	700 °C	600 °C
Bias voltage	−100 V	−70 V	−100 V	−70 V
Frequency	1 kHz	1 kHz	1 kHz	-
Deposition time	225 min	225 min	225 min	170 min
Power	5 kW			
Deposition pressure	4–8 Pa			
Target-substrate distance	20–30 mm			
Table rotation speed	2 rpm			

Table 2
Overview of the electrical resistivity and the CTE of the used substrates and TiAlN interdiffusion barrier.

Material	Electrical resistivity	CTE
IN718 [27]	$\rho_{RT} = 1.21 \cdot 10^{-6} \Omega m$	$\alpha_{RT-900°C} = 12.8 \cdot 10^{-6} K^{-1}$ - $17.2 \cdot 10^{-6} K^{-1}$
WC–Co [29,30]	$\rho_{RT} \approx 0.18 \cdot 10^{-6} \Omega m$	$\alpha_{600°C} = 6.0 \cdot 10^{-6} K^{-1}$ - $7.0 \cdot 10^{-6} K^{-1}$
Rubalit®708HP [28]	$\rho_{RT} = 10^{11}\ \Omega m$	$\alpha_{RT-800°C} = 7.0 \cdot 10^{-6} K^{-1}$ - $9.0 \cdot 10^{-6} K^{-1}$
TiAlN [31–33]	$\rho_{RT} = 1.9 \cdot 10^{-5} \Omega m$ - $4.6 \cdot 10^{-5} \Omega m$	$\alpha_{RT-600°C} = 6.4 \cdot 10^{-6} K^{-1}$ - $10.2 \cdot 10^{-6} K^{-1}$

30 µm × 35 µm (width × height × depth) volumes at both long sides utilizing a JEOL JIB-4610F focused ion beam device, resulting in a transmission length of approx. 130 µm. Fig. 1b shows the top view of the prepared sample.

The small beam size of only 0.4 µm × 0.4 µm enabled a high spatial resolution and thereby the separate depth-resolved investigation of the Cr-Al-C and TiAlN coatings. To achieve a high resolution and sufficient scattering vector Q range for phase analysis, the energy of approx. 24.6 keV in combination with the Photonics Science Imagestar 9000 area detector – 2940 pixel × 2940 pixel with 61 µm × 61 µm pixel size – was used. The experiments were performed in transmission mode with the beam direction parallel to the coating's surface. Fig. 1a gives an overview of the experimental arrangement. The sample-detector distance was about 221 mm with a maximum resolution of 0.02 °/pixel and ΔQ = 0.03 nm^{-1}. The depth scan was carried out from the top to the substrate with a step size of 0.4 µm, a counting time of 300 s for each image, and at least 32 steps per sample. The sample alignment was supported by one camera in the beam direction (y-axis), facilitating a precise alignment in the z-direction and the sample rotation about the y-axis. However, the alignment of the sample rotation about the x-axis could not be verified accurately and thereby all samples were slightly tilted. Due to the high transmission length compared to the thin coating, a small tilt angle of approx. 3° results in a diagonal beam path, so that one measurement step comprises information of the near-surface region and the coating-substrate interface. As a result, most P03 frames showed intensities of the substrate for the near-surface measurement as well. Even though the small tilt angles result in integral information of the coating's top, middle, and coating-surface interface region, due to the small tilt angles, the ratio of each region will nevertheless vary over the whole step scan, as the results in Section 3.2.1 show.

Since synchrotron experiments are limited in time, not every coating-substrate combination could be investigated, and only the results of DCMS-600 and HPPMS-600 coatings are presented.

To investigate the strain state of the as-deposited and tempered state of the Cr-Al-C coatings, in situ X-ray cross-section experiments were performed at the high energy materials science beamline P07 operated by the Helmholtz-Zentrum Hereon at the light source PETRA III at DESY, Hamburg [35] – henceforth referred to as P07 experiment. The transmission experiments were performed with a synchrotron beam size of 400 µm × 100 µm (width x height) with an energy of 87 keV, enabling a very high time and temperature resolution during heating and cooling. The beam direction was parallel to the coating's surface. In order to reduce the intensities of the substrate, the sample was adjusted vertically so that approx. half of the 100 µm beam was above the coating's surface. The distance of the sample to the used PerkinElmer XRD 1621 CN3 detector – 2048 pixel × 2048 pixel with 200 µm × 200 µm pixel size – was 1745 mm, resulting in a resolution of 0.007 °/pixel and ΔQ = 0.05 nm^{-1}.

The 10 mm × 5 mm × 1 mm (length x width x height) samples were heat-treated in a temperature range of RT - 900 °C utilizing a DIL805 A/D dilatometer from TA Instruments (formerly Bähr-Thermoanalyse GmbH). The dilatometer had two Kapton windows for the incoming and outgoing beam, with an induction coil with cooling channels for fast air cooling. The temperature and time accuracy is specified as ΔT = 0.05 K and Δt = 0.0005 s. A Typ S thermocouple was attached to the bottom of the sample for temperature control. The dilatometer was first evacuated and then flooded with Argon. Fig. 1c gives an overview of the experimental setup in the dilatometer. In order to increase the dynamic range of the detector, each diffraction image comprised the sum of 40 single images (20 bright and 20 dark) with 0.25 s exposure time for IN718 and 0.5 s for WC–Co for every single image. For WC–Co the exposure time had to be increased because of the higher absorption. With the constant heating and cooling ramp of 30 K/min, the time steps in which the images were measured correspond to a temperature step of approx. 6 K and 11 K for IN718 and WC–Co samples, respectively.

The presented P07 experiment results are obtained by different heat treatments. Table 3 summarizes these heat treatments and the respective indices used in Section 3.3.

Analysis of the synchrotron diffraction images from both synchrotron experiments and preparation for further investigations – frame integration and slicing – was performed with the software FIT2D [36,37]. Analysis of the integrated synchrotron diffraction images and X-ray diffraction pattern was performed with Match!3 from CRYSTAL IMPACT [38] and TOPAS 6 from Bruker Corporation for phase identification and Rietveld Refinement. The phases Cr_2AlC [39], Cr_7C_3 [40], and $(Cr,Al)_2C$ [41] were calculated on basis of data from Springer Materials. The data for the crystallographic structure of the substrates were used from data provided by Match!3 on basis on the Crystallography Open Database (COD) [42].

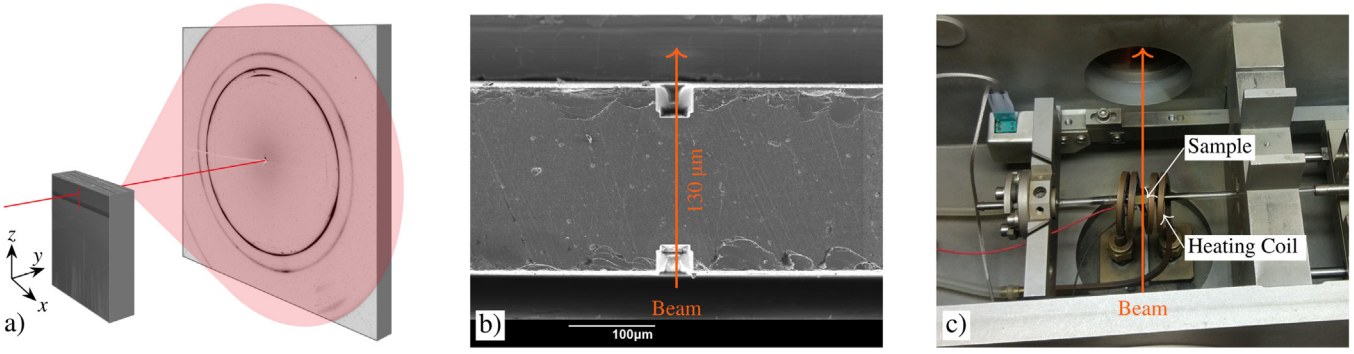

Fig. 1. (a) Overview of the P03 experiment with beam, sample, and detector assembly, (b) top view of the P03 sample after FIB preparation, and (c) overview of the sample adjustment in the dilatometer of the P07 experiment.

Table 3
Overview of the different P07 experiment heat treatments and analysis temperatures with the respective indices used in Section 3.3.

Heat treatment	Temperature of analysis	Index
Cyclic – heat to 700 °C & cool to 100 °C	after first heating at 700 °C	–700 °C
Cyclic – heat to 700 °C & cool to 100 °C	after first cooling at 100 °C	–100 °C
Cyclic – heat to 900 °C & cool to 100 °C	during first heating at 750 °C	–750 °C
Isothermal – heat to 700 °C/ 2 h dwell time	after 2 h dwell time at 700 °C	–700 °C/2 h

Because the two synchrotron experiments P03 and P07 were performed with different photon energies, the results in this paper are given in fundamental unit $Q = 4\pi\frac{sin(\theta)}{\lambda}$ to obtain comparability.

2.2.3. Nanoindentation

The indentation hardness H and Young's modulus E of the coatings were determined using the ZHN nanomechanical hardness tester from the ZwickRoell Group, Germany. To ensure a sufficient stiffness of the measurement system device-sample-holder, the samples were fixed with rosin on a steel cylinder, attached with screws in a sample holder to inhibit lateral and vertical movement of the samples during the measurement. A slight smoothening process with a rotating cemented carbide ball (ø = 20 mm) was carried out on each sample to minimize surface roughness for the subsequent indentation process and to reduce the measurement error.

A diamond Berkovich indenter from Synton-MDP LTD Nidau, Switzerland (E = 1140 GPa, ν = 0.07) was loaded to a maximum force between 35–200 mN using the quasi-continuous stiffness method (QCSM [43]). The measurement was evaluated according to ISO 14577–4 and the Oliver–Pharr technique [44]. According to the QCSM-method, the measurement force is increased in small steps. For each step during a dwell time of approx. 1.4 s the force oscillated with f = 40 Hz. With this method, it is possible to obtain a depth-resolved measurement of hardness and Young's modulus. At least 25 indentations were performed on each sample. After the indentation process, H and E were determined for every single indentation. After that, the single H and E values were averaged.

For evaluation of the hardness and Young's modulus values, the InspectorX version 4 software from the ZwickRoell group was used. Before each indentation procedure, a so-called area function calibration was carried out by indenting the same load as for the coating analysis into a calibration setup containing Sapphire (E = 410 GPa, ν = 0.234) and Quartz (E = 71.5 GPa, ν = 0.17) samples. For both calibration materials, the area function of the nanoindenter tip was evaluated and stored in a configuration file, which was used during the indentation procedure of the coating. An often-repeated calibration gives the possibility to control the condition of the tips and information of the tip radius, which should not exceed 200 nm.

The hardness values were obtained at the plateau of constant hardness over depth. Only in this region, the coating hardness can be derived. According to ISO 14577–4, a linear fit and an extrapolation to contact radius = 0 were used to determine Young's modulus of the coatings.

2.2.4. Annealing post-treatment

An annealing post-treatment of the as-deposited coatings at 800 °C and 1 h dwell time was carried out in order to investigate the microstructure and phase composition after the finished Cr_2AlC phase formation. The samples were heated with 10 K/min to target temperature in a tube furnace and furnace cooling was used. During the treatment, the samples were shrouded by constant argon flow.

3. Results and discussion

3.1. Analysis of microstructure and elemental composition

3.1.1. Microstructure

Fig. 2 shows the cross-section of the HPPMS-600 (Fig. 2a), HPPMS-600/-70 V (Fig. 2b), HPPMS-700 (Fig. 2c), and DCMS-600 (Fig. 2e) coatings in the as-deposited state on WC–Co with a TiAlN

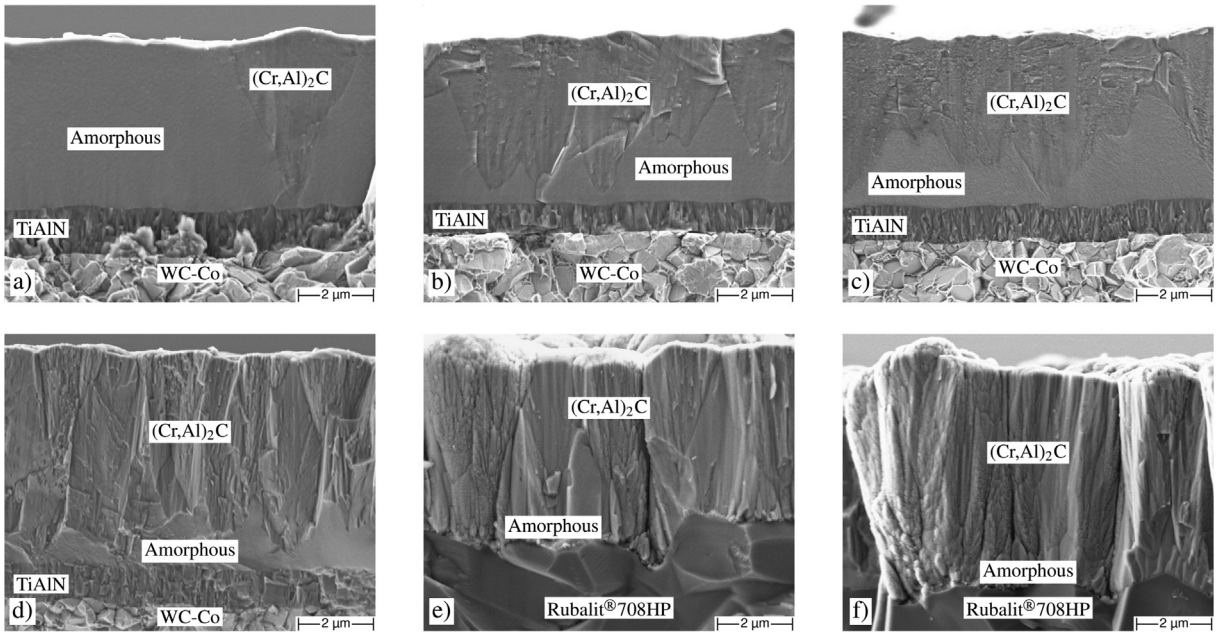

Fig. 2. SEM cross-section images of cryo-cracked (a) HPPMS-600, HPPMS-600/-70 V, (c) HPPMS-700, and (d) DCMS-600 coatings with TiAlN interdiffusion barrier on WC–Co substrate and e) HPPMS-600 and f) DCMS-600 coatings on Rubalit®708HP in the as-deposited state.

interdiffusion barrier. While the HPPMS coatings are on average 4.6 μm in thickness, the DCMS-600 coating is 5.7 μm on average. Cr-Al-C coatings consist of crystalline, cone-like shaped, and amorphous areas (see Section 3.2.1 for phase analysis). The amorphous areas can be distinguished by the absence of structural information and the lighter gray tone as a result of the channeling effect. In crystalline phases, crystallographic planes can act as channels increasing electron penetration depth before interactions and hence reducing the signal gathered with detectors. In contrast, short-range ordering of amorphous matter leads to increased near-surface information which results in a brighter tone [45]. As described further in Section 3.2.1 the crystalline phase was identified as the metastable $(Cr,Al)_2C$ phase.

As to be seen in Fig. 2 the HPPMS-600 coating is mainly composed of an amorphous phase. The decrease of the Bias voltage in the case of HPPMS-600/-70 V and the increase of the chamber temperature for HPPMS-700 result in increased volumes of $(Cr,Al)_2C$ for both coatings. The highest amount of the crystalline phase for the Cr-Al-C coatings on the substrates with low electrical resistivity, IN718 and WC–Co (see Table 2), was determined for DCMS-600, with the amorphous phase only located at the coating-TiAlN interface. It was found that the microstructure, as well as the elemental and phase composition, did not show differences between IN718 and WC–Co substrates.

The microstructure of the HPPMS-600 and DCMS-600 coatings on Rubalit®708HP (Fig. 2e and Fig. 2f) did not show the same pronounced differences as for the IN718 and WC–Co substrates. While the same dependency of the coating thickness on the HPPMS and DCMS process was determined for all substrates, the coatings on Rubalit®708HP show a broad, columnar structure and high amount of $(Cr,Al)_2C$ independent of the deposition process. As for the other two substrates, the comparison of the two images Fig. 2e and Fig. 2f may suggest a lower amorphous amount for the DCMS-600 coating, located only near the coating-substrate interface compared to HPPMS-600. However, these differences are not as dominant as for the other substrates and may also depend on the position of the cross-section and no distinct differences in the diffraction pattern were found (see Section 3.2.1).

The cone-like shaped $(Cr,Al)_2C$ and amorphous areas prove that the thermal energy at the substrate surface and kinetic energy of the sputtered flux were not sufficient for neither an entire crystalline coating nor the Cr_2AlC formation (see Section 3.2.1). The shape of crystalline areas indicates heterogeneous nucleation at preferred sites at the TiAlN interdiffusion barrier, from where the crystalline areas had grown further in height and width. In Fig. 2a and Fig. 2e the contact to the interdiffusion barrier is apparitional.

In PVD processes the resulting energy for the coating growth – kinetic energy of the sputtered flux and thermal energy on the substrate surface – is always a combination of different process parameters. Among others, the PVD-process (DCMS or HPPMS) with the bias voltage (for the ionized matter) determines the kinetic energy of the sputtered flux and thereby the impact on the substrate and growing coating. Higher kinetic energy increases the surface temperature, induces stress as well as collisions of the sputtered flux with surface atoms. As a result, the adatom mobility is increased and phase formation/crystallization may be possible at lower substrate temperatures [18]. However, the high energy provided by the HPPMS process in combination with high bias voltage leads to increased renucleation, which provides the known dense structure with inhibited columnar grain growth [19,46]. The fine-grained microstructure of the crystalline areas of the HPPMS-700 coating in Fig. 2c compared to the broader columnar microstructure for DCMS coating in Fig. 2e show this effect very clearly. However, as the low crystalline amount for HPPMS-600 shows, if the provided thermal energy is too low for a high number of growable heterogeneous nucleation sites, restraining grain growth lead to mainly amorphous coatings.

The comparison of the three HPPMS coatings on substrates with low electrical resistivity clearly shows how Bias voltage and chamber temperature determine the coating's morphology. The increased chamber temperature to 700 °C for HPPMS-700 provided higher thermal energy at the substrate surface, resulting in a higher density of growable nuclei and thereby enhanced crystallinity of the coating. In the case of the HPPMS-600/-70 V coating, the reduced Bias voltage results in lower kinetic energy of the sputtered flux, whereby the restrain of the nuclei growth is reduced, resulting in an increased coating crystallinity. As already pointed out, the energy of sputtered flux during the DCMS deposition process can be lower by a few orders of magnitude compared to the HPPMS process [18,20]. For that reason the restrain of the nuclei and grain growth is highly reduced, resulting in the highest crystallinity among all coatings on the substrates with low electrical resistivity.

As the effect of Bias voltage for the acceleration of the ions in the sputtered flux highly depends on the electrical resistivity of the substrate, the impact of the deposition process on the kinetic energy of the sputtered flux is distinctively decreased for substrates with high electrical resistivity like Rubalit®708HP (see Table 2). Without the effect of Bias voltage, the kinetic energy of the highly ionized sputter flux – hence the bombardment of the growing coating – of the HPPMS process is reduced, which results in less pronounced differences between the HPPMS-600 and DCMS-600 coatings on Rubalit®708HP.

3.1.2. Elemental composition

Table 4 summarizes the Cr and Al content of both, the crystalline and amorphous areas for the three Cr-Al-C coatings. The C content was not determinable due to the necessary deposition of the samples with a thin carbon film in order to perform the SEM and EDS analyses at high magnification. The DCMS-600 coating shows a decreased Cr/Al ratio compared to the HPPMS coatings. This is a common effect if the same target is used for both deposition processes. The main reason is the increased selective resputtering of Al for the HPPMS coatings due to ion bombardment on the growing coating – mainly Ar + and Ar^{2+} ions for DCMS and Cr^+, Al^+, Ar^+ and Ar^{2+} ions for HPPMS [18,20]. The HPPMS process is known for the high kinetic energy and ionization rate of the sputtered flux during the duty cycles, which combined with a high bias voltage, increases the ion bombardment in comparison to the DCMS process by a considerable amount for substrates with sufficient electrical conductivity [18,20]. Additionally, due to the larger amount of ionized Al in the vicinity of the target, the redirection of these ions to the target and the self-sputtering may contribute to the decreased Al content as well [18]. The resputtering and self-sputtering of Al are favored because of its lower atomic mass compared to Cr and the almost ten times higher Ar + sputtering and self-sputtering yield (calculated values of $\gamma_{Al}^{Ar^+} = 0.306, \gamma_{Al}^{Al^+} = 0.462$ and $\gamma_{C}^{Ar^+} = 0.032$ [18]) compared to the lighter C atoms. Additionally, Al has the lowest surface binding energy of the three elements. [20,47].

In comparison with the crystalline areas, the EDS results show up to 3 at.% higher Cr content for the amorphous areas. Considering the presence of amorphous areas in the coatings, a diffusion-related origin is not likely. While effects related to the measurements like the channeling effect and/or different surface oxidation – as the result of different bonding and diffusion in the crystalline and amorphous phase at room temperature – may influence the measurement, results of a subsequent heat treatment prove a deposition related origin. As described for the compositional differences in crystalline areas between DCMS and HPPMS coatings, dif-

Table 4
Cr and Al content of the Cr-Al-C coatings obtained by cross-section EDS analysis for crystalline and amorphous areas. The values for Cr and Al in at.% consider only the Cr/Al ratio without C.

	HPPMS-600		HPPMS-700		DCMS-600	
	crystalline	amorphous	crystalline	amorphous	crystalline	amorphous
Cr in at.%	66.9	69.9	68.9	69.5	62.3	65.5
Al in at.%	33.1	30.1	31.1	30.5	37.7	34.5
Cr/Al ratio	2.02	2.32	2.21	2.28	1.65	1.89

ferent re- and self-sputtering of Al during coating growth may lead to these variations. Resputtering depends among others on bonding between elements and grain orientation, which are different for amorphous and crystalline phases [48].

In order to investigate this effect, the coatings were heat-treated at 800 °C for 1 h dwell time (see Section 2.2.4). During the heat treatment, the formation of Cr_2AlC and Cr_7C_3 occurred. Fig. 3a to Fig. 3c show the cross-section of the three different coatings and Table 5 the estimated fractions of Cr_2AlC and Cr_7C_3 for the two areas after the heat treatment. Area 1 and Area 2 correspond to the former crystalline $(Cr,Al)_2C$ and amorphous areas in Fig. 2 in Section 3.1.1, respectively. The phases were identified by the analysis of heat-treated samples from P03 synchrotron transmission experiments and surface X-ray diffraction measurements in common reflection geometry with $Cu - K_\alpha$ radiation. With the consideration of an error of $\approx \pm 5$ % for the image analysis – derived from the analysis approach and possible influence of the location of the cross-section for Area 1 –, the results confirm a higher Cr_7C_3 amount in Area 2 for all three coatings. Those are the result of the higher Cr content, measured for amorphous areas in the as-deposited state (see Table 4). A further discussion of these results is given in the second paper of the series [26] to keep this part focused on the as-deposited state.

3.2. Analysis of phase composition and lattice parameter determination

3.2.1. Phase composition

Fig. 4 and Fig. 5 show the diffraction images with Debye–Scherrer rings of HPPMS-600 and DCMS-600 coatings on WC–Co and Rubalit®708HP, respectively, obtained from P03 experiment depth scans. The integrated diffraction pattern of each image is placed at the bottom of the corresponding diffraction image. The horizontal and vertical azimuth directions in the images are nearly parallel and perpendicular to the coating surface, respectively. Utilizing the small beam size of 0.4 µm × 0.4 µm of the P03 beam line enabled the measurement of almost whole Debye–Scherrer rings – WC–Co substrate resulted in shadowing in the 180° - 360° azimuth range. Due to the shadowing of the WC–Co substrate, the integration of these diffraction images was performed in the azimuth range 0°-180° – with 0° at the horizontal right and vertical center of the images – while the integration for Rubalit®708HP was performed from 0°-360°. Even though the beam size was small and below the size of crystalline areas (see Fig. 2), with the transmission length of approx. 130 µm and apparent small grain size in crystalline areas, the scattering information comprises a sufficient number of grains. Therefore, the following results reflect the state of the whole coating.

Fig. 4a, Fig. 4c, Fig. 5a, and Fig. 5c correspond to the near-surface region and Fig. 4b, Fig. 4d, Fig. 5b, and Fig. 5d to the region near the coating-substrate interface of the HPPMS-600 and DCMS-600 coatings. As described in Section 2.2.2, the samples were slightly misaligned thus the tilt about the x-axis (see Fig. 1a) resulted in a diagonal path of the synchrotron beam through the coating, whereby the top and the bottom diffraction images contain reflections from the WC–Co or Rubalit®708HP substrate. The substrate diffraction peak intensities increased with the depth step. The (111) and (200) reflections of TiAlN were visible for the HPPMS-600 and DCMS-600 coatings in Fig. 4b and Fig. 4d. As to be seen in all diffraction images in Fig. 4 and Fig. 5, the crystalline phase was identified as metastable $(Cr,Al)_2C$, as observed in earlier studies for Cr-Al-C PVD coatings [19].

Currently, two metastable phases are proposed in the literature. Shtansky et al. [19] described the $(Cr,Al)_2C$ phase in as-deposited coatings and Abdulkadhim et al. [22] proposed the metastable $(Cr,Al)_2C_x$ phase on basis of an ab initio calculation as an intermediate phase during the Cr_2AlC formation from amorphous Cr-Al-C coatings. The $(Cr,Al)_2C$ solid solution originates from the hexagonal Cr_2C phase (space group $P6_3/mmc$, prototype Mo_2C [21]), where both Al and Cr are randomly distributed at the Cr-sites (Wyckoff position 2c - 1/3,2/3,1/4) [19,41]. The $(Cr,Al)_2C_x$ phase is described as disordered Cr_2AlC with the same space group and prototype as $(Cr,Al)_2C$. However, the disordered state is not described in more detail in [22] and no information is given on whether the Al and Cr atoms share the same positions in this unit cell as described for $(Cr,Al)_2C$. Because the $(Cr,Al)_2C$ and $(Cr,Al)_2C_x$ phases have a similar crystal structure, both metastable phases share essentially the same diffraction peaks, with slightly different diffraction peak positions due to the different determined lattice parameter – $(Cr,Al)_2C$ with a = 2.79 Å and c = 4.46 Å [19], $(Cr,Al)_2C_x$ with

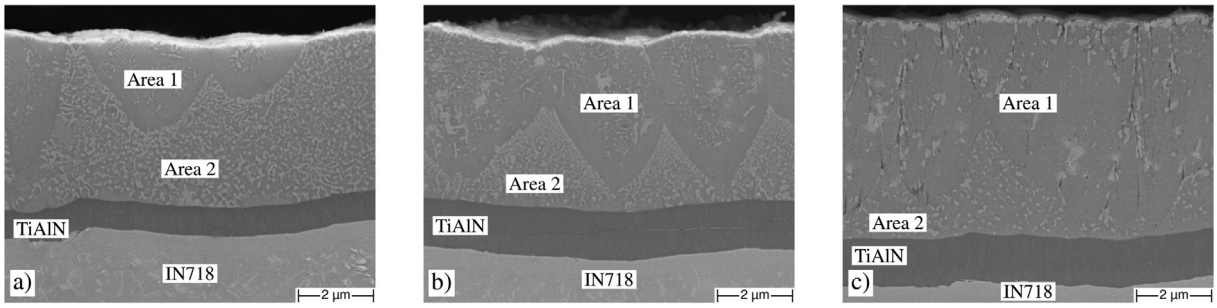

Fig. 3. SEM cross-section images of ground (a) HPPMS-600, (b) HPPMS-700, and (c) DCMS-600 coatings with TiAlN interdiffusion barrier on IN718 substrate after heat treatment at 800 °C for 1 h dwell time.

Table 5
Average Cr_2AlC and Cr_7C_3 amounts for the two areas in Fig. 3 for HPPMS-600, HPPMS-700 and DCMS-600 coatings after heat treatment at 800 °C for 1 h dwell time. Values were determined by analysis of SEM cross-section images using the Fiji-ImageJ software with the Trainable Weka Segmentation Plugin [49,50]. The error is estimated ±5 %.

	HPPMS-600		HPPMS-700		DCMS-600	
	Area 1	Area 2	Area 1	Area 2	Area 1	Area 2
Cr_2AlC in vol%	88	62	77	64	91	86
Cr_7C_3 in vol%	12	38	23	36	9	14

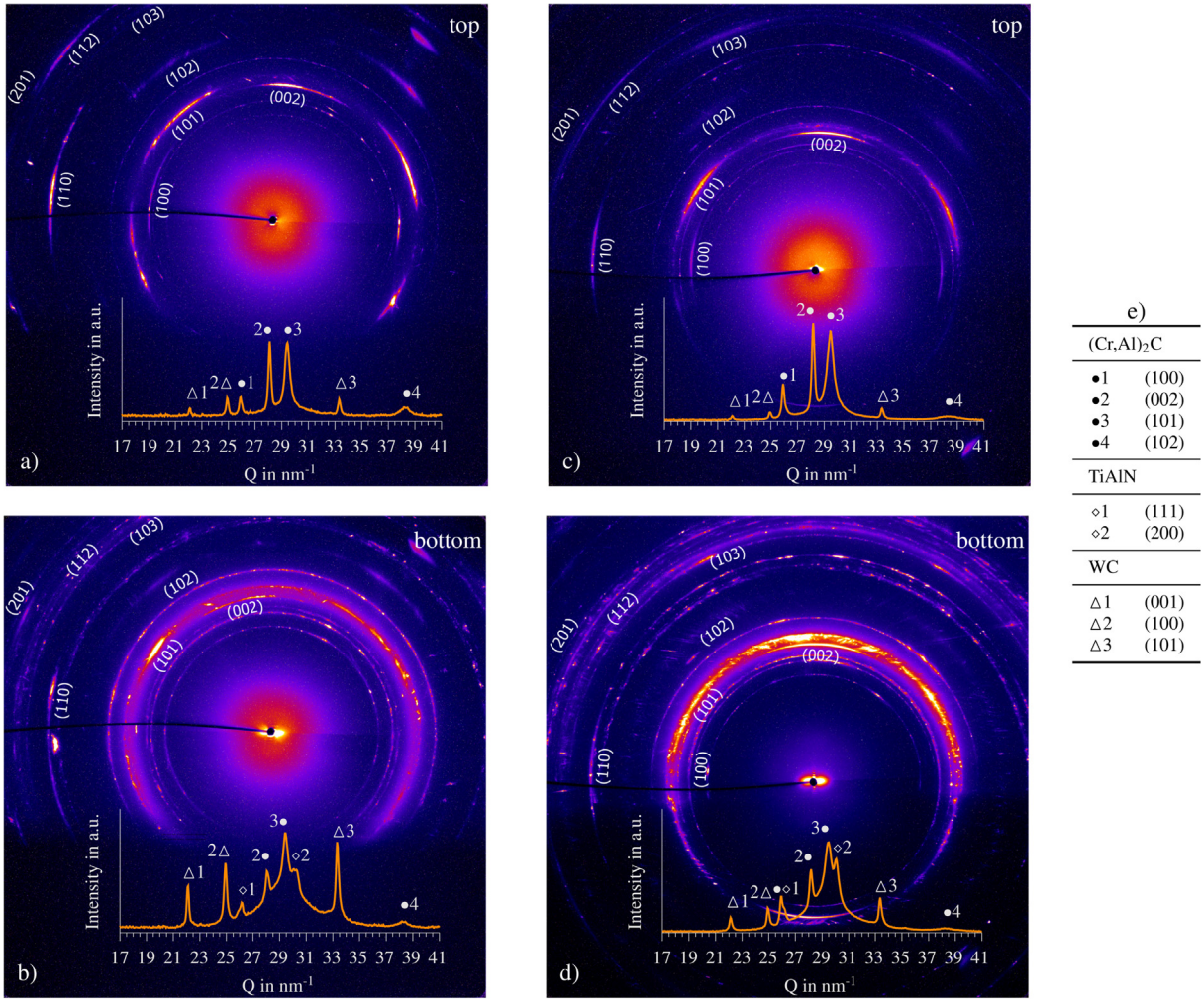

Fig. 4. P03 diffraction images with Debye–Scherrer rings and labels of crystallographic planes of $(Cr,Al)_2C$ (calculated on basis of structural data from [41]) and diffraction pattern, integrated over the azimuth range 0° to 180°. a) and b) show the top and bottom region of the HPPMS-600 coating and (c) and d) the top and bottom region of the DCMS-600 coating on WC–Co. (e) summarizes the reflections marked in the integrated diffraction pattern in (a), (b), (c), and (d). Each diffraction image was processed separately with a unique color scale with Fiji ImageJ [50] and thereby image intensities are not comparable.

a = 2.825 Å and c = 4.353 Å [22]. In particular, the small lattice parameter c of the two metastable phases results in the shift of the (002) and (101) reflection to higher Q values – $Q_{(002)-(Cr,Al)_2C} \approx 28.0\ nm^{-1}$ and $Q_{(002)-Cr_2AlC} \approx 9.5\ nm^{-1}$, $Q_{(101)-(Cr,Al)_2C} \approx 29.5\ nm^{-1}$ and $Q_{(101)-Cr_2AlC} \approx 25.5\ nm^{-1}$ –, whereby these two diffraction peaks are the distinctive feature for ordered Cr_2AlC.

As described in the second paper of the series [26], during the P07 in situ investigations (see Section 2.2.2), a different metastable disordered-Cr_2AlC phase (dis.-Cr_2AlC) was found as the intermediate phase for Cr_2AlC phase formation. Dis.-Cr_2AlC shows the same crystal structure as Cr_2AlC with decreased lattice parameter a and increased lattice parameter c ($a_{dis-Cr_2AlC\ at\ 677\,°C}$=2.845 Å and $c_{dis-Cr_2AlC\ at\ 677\,°C}$=13.285 Å to $a_{Cr_2AlC\ at\ 843\,°C}$=2.895 Å and $c_{Cr_2AlC\ at\ 843\,°C}$=12.995 Å [26]), resulting from the Al positions not occupied properly (Wyckoff position 2c - 1/3,2/3,1/4 [39]). The disordered state of the Al atoms in the unit cell leads to a pronounced decrease in the intensities of the characteristic (002) and (101) Cr_2AlC diffraction peaks, whereby these reflections are bare to not visible in the diffraction pattern. A similar phase was described by Zamulaeva et al. [16] for Cr_2AlC formation via pulsed electrospark deposition but is not yet considered as a intermediate or metastable phase during Cr_2AlC phase formation.

Additionally, only the dis.-Cr_2AlC phase was determined for the amorphous to Cr_2AlC phase formation during the P07 experiments, thus it is likely that the phase found by Abduhlkadhim et al. [22] during the phase formation is not the proposed $(Cr,Al)_2C_x$ with a small unit cell but the newly found dis.-Cr_2AlC phase [26]. For more information on that topic, the reader is referred to the second paper [26].

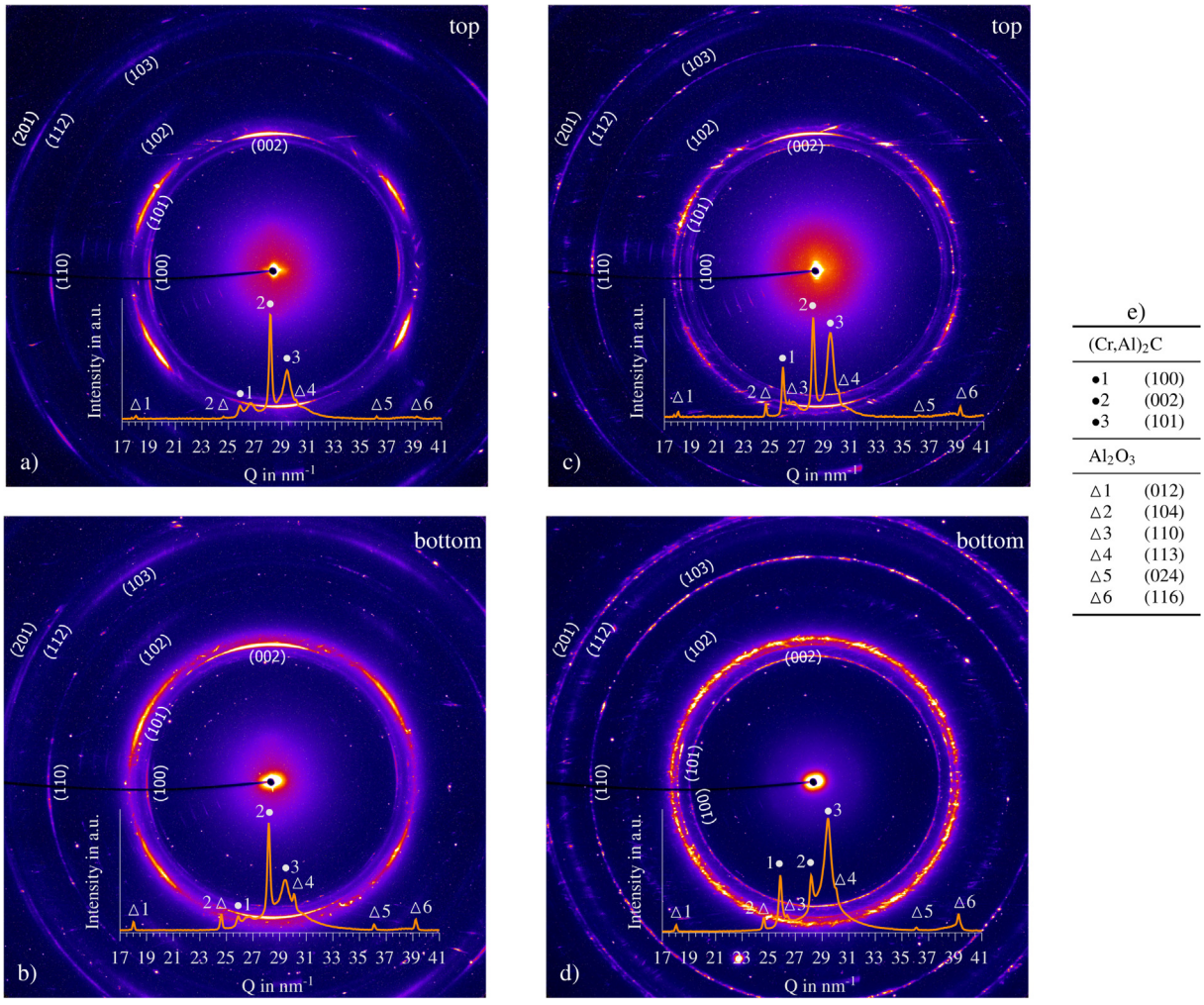

Fig. 5. P03 diffraction images with Debye–Scherrer rings and labels of crystallographic planes of $(Cr,Al)_2C$ (calculated on basis of structural data from [41]) and diffraction pattern, integrated over the azimuth range 0° to 360°. (a) and (b) show the top and bottom region of the HPPMS-600 coating and (c) and d) the top and bottom region of the DCMS-600 coating on Rubalit®708HP. e) summarizes the reflections marked in the integrated diffraction pattern in (a), (b), (c), and (d). Each diffraction image was processed separately with a unique color scale with Fiji ImageJ [50] and thereby image intensities are not comparable. The diffraction peak between $(Cr,Al)_2C$ (100) and (002) in a), b) and c) results from an Ag contamination from the sample preparation.

In this study, the metastable $(Cr,Al)_2C$ phase from Shtansky et al. [19] is used because, as described above, the structural information for this phase is available – which is necessary for the reflection calculation for different X-ray wavelength –, and this phase is described for the as-deposited state of Cr-Al-C coatings.

A pronounced (002) fiber texture of $(Cr,Al)_2C$ could be observed for all Cr-Al-C coatings, which is evident by the (002) intensity maximum in the range of the 90° azimuth direction (equals the vertical axis in the diffraction images). Even though the sample rotation about the surface normal (z-axis in Fig. 1a) was not possible due to used samples and thereby information from the third room direction is missing, the relation of the different planes in the diffraction images confirm this assumption. The appearance of the (100) and (110) reflections in the diffraction images – which are tilted against each other by approx. 30° around the < 002 > direction in the unit cell – in the azimuth range of 180°, implies a random grain orientation around the (002) normal. The basal plane in hexagonal unit cells is often characterized by the lowest surface energy [51] and thereby a (002) fiber texture is likely if the provided thermal energy at the substrate surface in the deposition process is too low for unhindered grain growth. Additionally, the c/a ratio of 1.60 for $(Cr,Al)_2C$ (see Section 3.2.2) is below 1.63, which is identified as a threshold for the basal plane fiber texture [52,53].

The slight tilt of the fiber axis may be attributed to a sample rotation in the experiment, the coating process as the result of an inclined sputter flux, or the growth direction of the nuclei and grains being slightly tilted. The last origin becomes visible when comparing the directions of the $(Cr,Al)_2C$ (002) intensity maxima between the top and bottom region for the HPPMS-600 coating in Fig. 4. The maximum in Fig. 4a is located at an azimuth of approx. 84°, while the azimuth for the (002) maximum in Fig. 4b is at approx. 96°, indicating different tilt angles of the measured coherent crystalline volumes.

It is interesting to note, that the (002) fiber texture is almost not visible for the bottom region for the DCMS-600 coating on Rubalit®708HP. While weak $(Cr,Al)_2C$ (002) intensity maxima are visible in the 90°/270° azimuth directions – possibly from the slight sample tilt –, an almost complete ring for the (002) reflection is visible too, indicating coherent diffraction volumes with different orientations compared to those in the near surface region. As described in Section 3.1.1, the inherent lower kinetic energy of the sputtered flux of the DCMS process in combination with the reduced acceleration of the ions through the Bias voltage for Rubalit®708HP – due to the high electrical resistivity – results in an increased number of

heterogeneous nucleation sites at the substrate surface. However, because the substrate temperature was too low for the unhindered growth of all nuclei and grains, those oriented with the (002) plane aligned almost parallel to the surface were favored to grow, as described above.

As described in Section 3.1.1, an amorphous phase was found besides the $(Cr,Al)_2C$ phase in the Cr-Al-C coatings. Because an amorphous phase does not show any discrete diffraction peaks in the diffraction pattern, this phase can be determined by the increase of the background, usually in the Q range of the main peaks, extending over several nm^{-1}. The amorphous phase was determined by the comparison of the integrated top and bottom diffraction images in Fig. 4 and Fig. 5 for the HPPMS-600 and DCMS-600 coatings, respectively. In particular for the WC–Co substrate a pronounced increase of the background in the Q range of approx. 25 nm^{-1} to 35 nm^{-1} in the integrated bottom diffraction pattern and a broad ring in the range of the $(Cr,Al)_2C$ (101) interference in the associated diffraction images could be determined. These results confirm the assumptions made in Section 3.1.1, where the amount of the amorphous phase increased towards the coating-substrate interface. The quantification of the coating's phase composition over the coating depth by Rietveld refinement was not reasonable because no calibration standard with a known amorphous to $(Cr,Al)_2C$ ratio was available.

In comparison to the available literature, even the chamber temperature of 600 °C exceeds the lowest reported temperatures for pure crystalline $(Cr,Al)_2C$ of 300 °C [19] and crystalline Cr_2AlC of 450 °C [13] significantly. However, the X-ray diffraction pattern published by Walter et al. [13] are possibly not correctly interpreted, as the metastable $(Cr,Al)_2C$ phase was not known at that time. The diffraction pattern for the proposed Cr_2AlC formation at 450 °C substrate temperature clearly shows the (100) and (002) $(Cr,Al)_2C$ diffraction peaks without the characteristic Cr_2AlC (002) and (101) reflections at lower Q values, as described earlier. Therefore, the substrate temperature for crystalline Cr_2AlC is 550 °C as the characteristic Cr_2AlC reflections are present in corresponding diffraction pattern [13].

Deposition in a science lab is often performed in smaller-sized coaters and sometimes in stationary mode to reduce deposition time and cost. In order to produce a high number of homogeneous coated samples in one batch, an industrial-sized coater was used. Samples were rotated around the center axis, whereby the actual time for the samples in the plasma in front of the two targets was only about 8% of the total deposition time (see Section 2.1). Therefore samples were cyclically heated and cooled resulting in a lower average deposition temperature. Despite the substrate temperature being controlled or measured for depositions from Shtansky et al. [19] and Walter et al. [13], the real substrate temperature is often higher and may reach peaks above the measured temperature at the immediate surface. In both studies, the DCMS process without the sample rotating out of the plasma was used. However, it is difficult to compare the different depositions, carried out in this and the mentioned studies, because several deposition parameters where different. For example, on the one hand, the deposition pressure of 4–8 Pa used in this study was about one magnitude higher (0.2 Pa in [19] and 0.6 Pa in [13]) resulting in a higher collisions probability, whereby the kinetic energy of the sputtered flux can be reduced. On the other hand, the target-substrate distance of 20–30 mm in this study is less than half compared to the 75 mm used in [13] (no information in [19]), which reduces the collision probability. Additionally, Walter et al. [13] used silicon substrates and Shtansky et al. [19] several different substrates, which may also influence the phase composition of the coatings, as described in Section 3.1. Therefore, it is difficult to derive a statement, why the chamber temperature of 600 °C or 700 °C did not resulted in pure crystalline $(Cr,Al)_2C$ or Cr_2AlC coatings.

The detrimental effect of a high Bias voltage and high kinetic energy of the sputtered flux on the formation of Cr_2AlC is reported in the literature [23,24]. Rueß et al. [23] determined the formation of $(Cr,Al)_2C$ for Bias voltage in the range of −200 V to −400 V, while at floating Bias Cr_2AlC was present. Additionally, the results show the beginning of the formation of $(Cr,Al)_2C$ for the HPPMS process already at −100 V Bias. While a comparison of the absolute values for the Bias voltage to the values used in this study is not reasonable because the other deposition parameters were different, the tendency that higher kinetic energy of the sputtered flux can hinder the formation of Cr_2AlC and crystalline phases is in line with results in this study.

The results in this section and Section 3.1 show, that for sputter processes the entirety of used materials, deposition processes, and deposition parameters determine the resulting coatings phase composition and microstructure. The reasons for metastable and amorphous coatings for deposition temperature at 600 °C and 700 °C in comparison to studies with crystalline Cr_2AlC at far lower temperatures (see Section 3.1.1) are tied to the following main factors.

- low average deposition temperature because of sample rotation,
- high bias voltage in combination with sufficient electrical conductivity for IN718 and WC–Co substrates,
- HPPMS process in combination with low average temperature and high bias voltage hinders the growth of crystalline nuclei.

3.2.2. Lattice parameter determination of $(Cr,Al)_2C$

Phase analysis held mainly two challenges, the coating inherent intrinsic and thermal residual stress, and the pronounced (002) fiber texture of the $(Cr,Al)_2C$ phase. Stress may shift the diffraction peaks and thereby increase or decrease lattice parameters. The texture complicates the finding of those stress effects because diffraction peaks are limited to certain azimuth ranges in the diffraction image. Therefore the direction-dependent investigation of the residual stress as in the case of thermal residual stress (see Section 3.3) with only one diffraction peak is not possible. Additionally, due to the lower crystallinity of the HPPMS-600 coating, the intensities are weaker in general.

In order to calculate the $(Cr,Al)_2C$ unit cell parameters a and c, the analysis of the diffraction images from the P03 experiments was performed in two steps to avoid misinterpretation due to influences of texture, residual stress and substrate. Analysis was performed for several depth steps for HPPMS-600 and DCMS-600 coatings on IN718, WC–Co and Rubalit®708HP substrates utilizing Rietveld refinement with the TOPAS6 software using the structural data of Cr_2C [41]. The HPPMS and DCMS deposition processes should result in different intrinsic residual stress, while the different CTE of the substrates should result in different thermal induced residual stress states (see Section 3.3). In order to analyze a possible azimuth dependency of the lattice parameter as the result of thermal residual stress, the diffraction images were sliced into 2° ranges in azimuth direction and integrated over Q in the first step. Lattice parameter a was calculated from (100) and (110) diffraction peaks at azimuth 180° ±10°, while lattice parameter c was calculated from (002) diffraction peak at azimuth 90° ±10°. To compare the values for direction dependence, the (101) diffraction peak at azimuth 151° ±10° and (103) at azimuth 122° ±10° – if present with sufficient intensity – were used for the Rietveld refinement with $a_{(100)/(110)}$ and $c_{(002)}$.

While a certain variation in the lattice parameters was detectable, no clear direction dependence was observed. Those variations

are attributed to the detector resolution limit of 0.02 °/pixel or 0.006 Å in combination with the small coherent scattering volume, Rietveld refinement, distortions as a result of the Al substitution in the unit cell, and deposition related distortion like point defects. Without the diffraction peak azimuth dependency, the diffraction images were integrated over the entire azimuth range for a and c calculation in the second step. The thus obtained higher intensities and number of diffraction peaks for the Rietveld refinement improved the fit. The results are summarized in Table 6 and are in good agreement with the currently available literature with $a = 2.78$Å $- 2.81$Å and $c = 4.39$Å $- 4.47$Å [16,19,22].

As to be seen in Table 6, no coating or substrate dependency was observed. However, with the wide CTE range of the substrates and different deposition processes, a difference in a and c for the coating-substrate combinations should be determinable. The absence of those will be discussed in Section 3.3.

3.3. Residual stress

As discussed in Section 3.2.2, the calculated lattice parameters did not show a distinct coating or substrate influence. Considering the used deposition processes and substrates, one should expect different residual stress states in the as-deposited state, resulting in different lattice parameters originating from the elastic strain. In the following, the residual stress of the 1st kind – resulting in a diffraction peak shift – will be discussed [54].

In order to investigate the residual stress state in this study, substrates with a wide range of CTE's (see Table 2) were used. However, because the as-deposited Cr-Al-C coatings contained an amorphous phase, the formation of Cr_2AlC or an intermediate phase was necessary. To lighten up the residual stress state of the as-deposited coatings and the influence of the deposition process and substrate, in situ heat treatment experiments up to 900 °C were performed at the Hereon beamline P07 at PETRA III, DESY. At first glance, an annealing post-treatment seems counterintuitive for the investigation of the as-deposited stress state. However, for reasonably short heating times at temperatures below plastic deformation, σ_{th} is reversible and σ_i does not undergo noticeable relaxation. Therefore, with the careful analysis of the temperature steps concerning the different stress origins, qualitative analysis is possible and can give insight into the as-deposited residual stress state. It turned out, that the newly found dis.-Cr_2AlC phase – briefly described in Section 3.2 and discussed in detail in the second paper of the series [26] – is present in the temperature range suitable for the stress analysis, therefore a brief overview of the dis.-Cr_2AlC formation is given in the following Section 3.3.2.

Due to the lack of knowledge of the elastic properties and X-ray elastic constants for the metastable phases in this study, the calculation of residual stress from measured strain is not possible in this work. Therefore, the discussion will be done qualitatively, based on the knowledge about intrinsic and thermal residual stress for PVD coatings.

3.3.1. Theoretical details for residual stress determination using X-ray diffraction

In general, the shift of diffraction peaks to higher Q values refers to compressive stress and lower Q values to tensile stress. Other effects on diffraction peak shifting, like composition gradients, could be excluded.

The total residual stress σ_{rs} in thin coatings can be described as the sum of three different origins as

$$\sigma_{rs} = \sigma_i + \sigma_{th} + \sigma_e, \tag{1}$$

where σ_i denotes intrinsic stress, σ_{th} thermal stress, and σ_e extrinsic stress [55].

The intrinsic residual stress σ_i arises from the accumulation of effects related to the energetic bombardment of the growing coating. Collision cascades of atoms and ions from the sputtered flux at and near the coating's surface generate various defects in grains and result in grain boundary densification induced by atom diffusion [56,57]. As a result, the atoms are displaced from their equilibrium positions causing elastic strain. If the film shows sufficient adhesion on the substrate, the hindered relieving causes residual stress [58]. The intrinsic residual stress highly depends on the deposition process and is usually compressive for dense coatings deposited at homologous temperatures T_S/T_m above 0.2 [59]. With regard to the deposition processes used in this study, the HPPMS process with the high kinetic energy of ionized sputtered flux, usually induces higher compressive residual stress compared to the DCMS process [60,61]. As a result, the diffraction peaks are shifted to higher Q values and the lattice parameter of the unit cell parallel to the surface should be smaller for HPPMS-600 or HPPMS-700 on the same substrate. However, with increasing temperature σ_i may be reduced as the result of thermally activated relaxation processes.

The thermal residual stress σ_{th} originates from a misfit of the CTE between substrate and coating in combination with a temperature different from the deposition [56]. For a coating-substrate combination with known coatings' Young's modulus E_c, Poisson ratio ν_c and the CTE's of the coating α_c and substrate α_s, the thermal stress can be calculated for the temperature difference between deposition T_d and measurement T as [55]

$$\sigma_{th} = \frac{E_c}{1-\nu_c}(\alpha_c - \alpha_s)(T_d - T). \tag{2}$$

Assuming sufficient coating to substrate bond for a thin coating, the substrate determines the expansion or contraction during heating and cooling. For a coating with a CTE higher than the substrate's CTE, compressive residual stress will arise during heating, whereas the cooling process will result in tensile residual stress. Without stress relaxation by diffusion processes at high homologous temperatures or plastic deformation, thermal stress is reversible.

The extrinsic residual stress σ_e originates from different processes like phase transformation, precipitation formation, plastic or creep deformation [62]. For the amorphous and metastable

Table 6
Lattice parameter of $(Cr,Al)_2C$ for HPPMS-600 and DCMS-600 coatings obtained by Rietveld refinement of integrated P03 synchrotron diffraction images. The given error was calculated from the detector resolution limit.

		IN718	WC–Co	Rubalit®708HP
HPPMS-600	a in $\pm 6 \cdot 10^{-3}$ Å	2.801	2.804	2.807
	c in $\pm 6 \cdot 10^{-3}$ Å	4.470	4.474	4.462
DCMS-600	a in $\pm 6 \cdot 10^{-3}$ Å	2.805	2.801	2.801
	c in $\pm 6 \cdot 10^{-3}$ Å	4.469	4.462	4.461

areas in the as-deposited coatings, extrinsic residual stress can be relevant for Cr_2AlC phase formation during post-deposition heat treatment, if a significant change in the volume occurs. However, as explained later in Section 3.3.2, the results do not give any evidence for a significant impact on the stress state compared to the thermal and intrinsic residual stress.

3.3.2. Residual stress in the as-deposited Cr-Al-C coatings

The heat maps in Fig. 6a - Fig. 6c show the amorphous to dis.-Cr_2AlC formation for the HPPMS-600 coating during the first heating cycle of the P07 experiment. Because the second paper of the series [26] is dedicated to the Cr_2AlC phase formation and gives more detailed insight, the description of the phase formation in this section only shows a small part of the results with respect to the stress state.

The formation of the metastable dis.-Cr_2AlC phase from the $(Cr,Al)_2C$ phase occurs at 632 °C, marking the start of the intermediate state of the Cr_2AlC formation. Fig. 6a shows this state of the Cr_2AlC formation at 663 °C. The emerging phase is referred to as disordered because of the splitting of (006) and (103) reflections resulting from an increased *c* lattice parameter compared to Cr_2AlC. The amorphous areas transform into dis.-Cr_2AlC at 677 °C, shown in Fig. 6b. The dis.-Cr_2AlC to Cr_2AlC formation starts at 695 °C and 801 °C for DCMS-600 and HPPMS-600, respectively. Even though the following results for DCMS-600 are acquired at 700 °C and thereby above the start temperature of the Cr_2AlC formation, only very small and barely determinable Cr_2AlC volumes are present at 700 °C and did not affect the analysis at this temperature. It has to be noted, that the dis.-Cr_2AlC to Cr_2AlC formation lasts from 695 °C to 801 °C for 212 s, while the heat treatment for the residual stress investigation was 6s for the temperature step 695 °C to 700 °C and 120 s dwell time at 700 °C. Therefore, the results in the following are related to the dis.-Cr_2AlC (103) reflection.

While the dis.-Cr_2AlC (103) is only barely detectable at 663 °C, the reflection is visible over the whole azimuth range at 677 °C and intensities increase further at 697 °C. The intensity evolution and distribution are influenced by the $(Cr,Al)_2C$ texture as well as the different amounts of the amorphous and $(Cr,Al)_2C$ phase in the as-deposited state. At 697 °C, a distinct azimuth dependence of the Q value of dis.-Cr_2AlC (100), (006), and (103) is observable, which is not present at 677 °C. Because those effects can't be the result of the 20 K temperature difference, they have to be related to residual stress present in the amorphous phase.

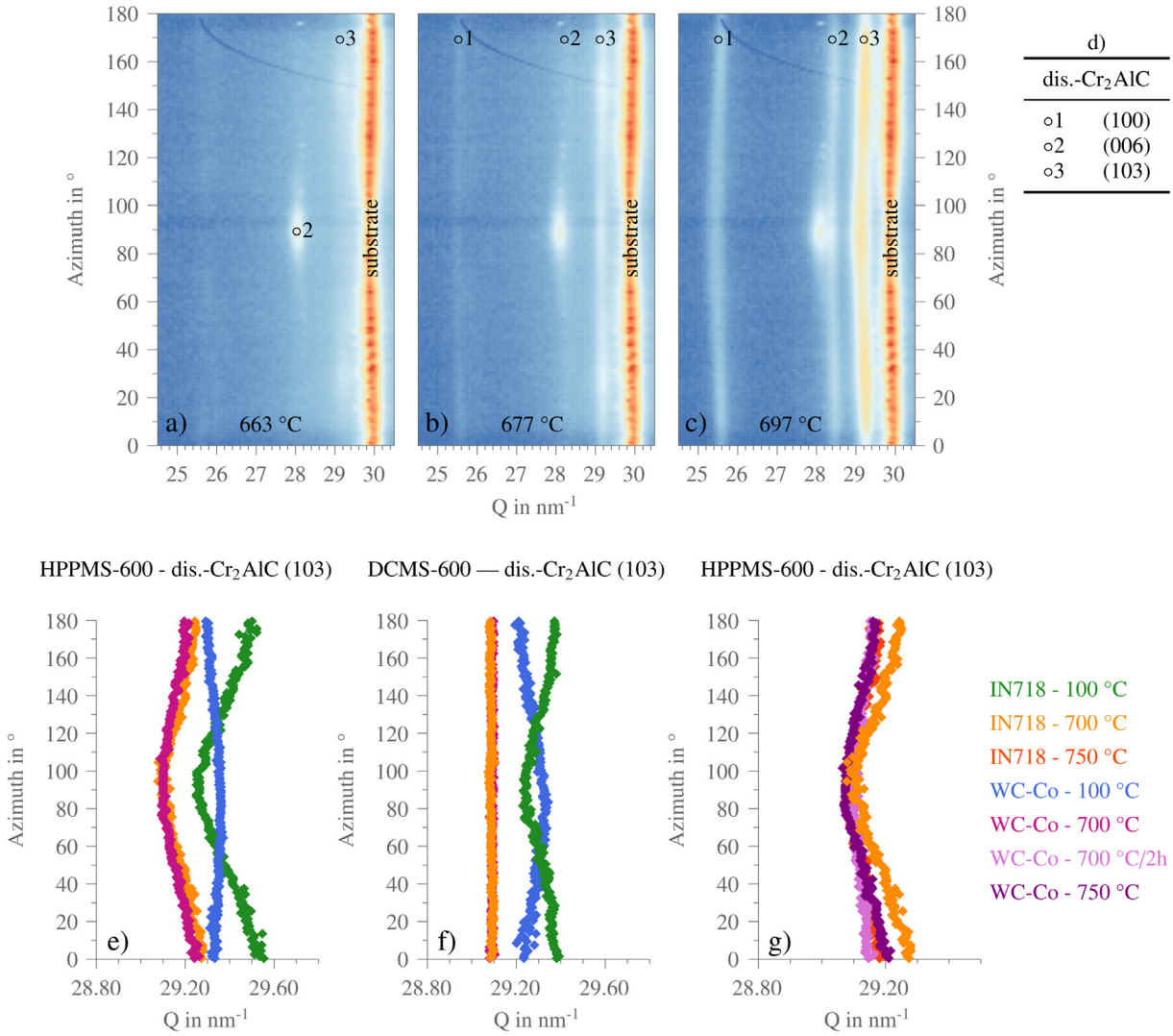

Fig. 6. Results of the in situ heat treatment measurements from the P07 experiments. (a) -(c) are the integrated diffraction images of HPPMS-600 on IN718 during first heating cycle at a) 663 °C, b) 677 °C and c) 697 °C, showing the azimuth dependence of Q of the reflections specified in d). The azimuth dependence of Q of the dis.-Cr_2AlC (103) reflection after heating to 700 °C and cooling to 100 °C is shown in e) for HPPMS-600 and in f) for DCMS-600 on IN718 and WC–Co. g) summarizes the results for HPPMS-600 on WC–Co for heating to 700 °C with 2 h dwell time and heating to 750 °C and on IN718 for heating to 700 °C and 750 °C.

The appearance of the (103) reflection at 677 °C is related to the nucleation and growth of the dis.-Cr_2AlC phase in the amorphous areas. At this point, a number of small grains – without a large distance connection to each other or the substrate – are not affected by the residual stress in the surrounding volume. However, with increasing temperature and time, ongoing phase formation – noticeable by the intensity increase – results in the bond of the dis.-Cr_2AlC grains and to the substrate/interdiffusion barrier surface. With the linkage to the surrounding material, relaxation is inhibited and the stress in the former amorphous volumes affects the newly formed phase, resulting in a Q shift and the bending of the reflection in Fig. 6c at 697 °C. It has to be noted, that due to the relatively high ramp of 30 K/min, the temperature step of 20 K comprises 40 s (equals 4 images), enabling the investigation of these time-sensitive processes.

To visualize the residual stress in the as-deposited state as well as the expected substrate and deposition process dependencies, the P07 Debye–Scherrer rings at the temperatures of interest were sliced into 1° steps in azimuth direction and integrated over Q. The Q position of the (103) reflection in dependence on the azimuth angle is shown in Fig. 6e and Fig. 6f for the substrates IN718 and WC–Co, at 700 °C and 100 °C. 700 °C refers to the first peak temperature of the first heat cycle and 100 °C to the lowest temperature of this cycle after cooling from 700 °C with 2 min dwell to 100 °C. As described earlier, σ_{th} depends on the difference of the measurement temperature to the deposition temperature. To prove that σ_{th} does not affect the residual stress state at 700 °C by a noticeable amount, additional samples were heated up to 750 °C. Additionally, to investigate a possible decrease of σ_i by thermally activated relaxation processes, additional samples were heat-treated isothermally at 700 °C for 2 h.

The results in Fig. 6g show that both, further heating and longer dwell time at 700 °C, decrease the azimuth dependence of (103) for HPPMS-600 coatings on IN718 and WC–Co. As explained in the following, the increased Q value in 0°/180° azimuth direction indicates planar compressive residual stress. Therefore the decrease of this azimuth dependency can be interpreted as the decrease of residual stress by thermally activated relaxation processes. With the maximum residual stress at around 700 °C, the stress state at this temperature can be assumed as mainly intrinsic deposition residual stress without significant thermal stress, because both substrates lead to different thermal stress during heating or cooling. Additionally, one can conclude that the compressive intrinsic residual stress from the deposition is not stable at 700 °C and thereby does not benefit coating lifetime for longer exposure times.

As to be seen in Fig. 6e and f, the intrinsic residual stress at 700 °C for the two coatings is significantly different. In the case of DCMS-600, the curves are almost identical for the different substrates without an azimuth dependence of Q. However, in the case of HPPMS-600, the (103) reflections are characterized by a pronounced increase of Q in azimuth 0° and 180° directions. The WC–Co curve is slightly shifted to lower Q values compared to the IN718 for HPPMS-600. Without the stress-free Q value, the distinction between compressive and tensile stress can be difficult. However, with the help of the DCMS-600 curves, at 700 °C the residual stress state is clear. The Q values of DCMS-600 at 700 °C ($Q_{IN718} = 29.09, Q_{WC-Co} = 29.10$) and HPPMS-600 at 700 °C in 90 ° direction ($Q_{IN718} = 29.13, Q_{WC-Co} = 29.14$) are very similar considering the detector resolution of about 0.05 nm^{-1}. The 90° azimuth direction or direction perpendicular to the surface can be assumed as almost stress-free. As discussed earlier, intrinsic stress is the result of energetic bombardment during deposition. The affected depth should be in the range of a few atom distances. While lateral relaxation is hindered by surrounding material, relaxation perpendicular to the surface is possible. Following this assumption, the increasing Q values for HPPMS-600 in 0° and 180° indicate planar compressive residual stress parallel to the surface.

After cooling to 100 °C, the results showed the expected substrate dependency. Even though the CTE for dis.-Cr_2AlC is unknown, it can be assumed that the CTE for this phase has to be similar to Cr_2AlC with $\alpha_{Cr_2AlC_{RT}} = 12.5 \cdot 10^{-6} K^{-1}$ [63] because both phases are only distinguished by slightly different lattice parameters and shifted Cr- and/or Al- sites [26]. As a result of the hindered contraction of the coatings on the WC–Co substrate, the development of tensile residual stress can be observed parallel to the surface. In difference, the higher CTE of IN718 compared to dis.-Cr_2AlC results in compressive stress during cooling because of the forced compression of the coating parallel to the surface. However, the interpretation for thermal stress without the stress-free Q value at 100 °C is more complicated. One can see, in difference to the 700 °C curves, the curves for 100 °C in Fig. 6e and Fig. 6f do not share similar Q values for any azimuth direction. These differences for thermal stress compared to the intrinsic deposition stress are the result of the different affected volumes. During cooling, assuming sufficient coating bond, the whole coating is either contracted or expanded parallel to the surface, resulting in a balancing strain component perpendicular to the surface. The coating thickness of approx. 5 µm is too high for the relaxation of this stress component, resulting in a triaxial stress state.

For the IN718 substrate, the compressive residual stress parallel to the surface is accompanied by tensile stress in a perpendicular direction. For WC–Co the arising residual stress is tensile parallel and compressive perpendicular to the surface.

The influence of the intrinsic residual stress of the HPPMS-600 and DCMS-600 coatings is visible for both substrates, by the different bending of the curves. The HPPMS-600 coating on IN718 shows higher compressive stress parallel to the surface at 100 °C compared to DCMS-600 as a result of the superposition of σ_i and σ_{th}, which are both compressive. In the case of HPPMS-600 on WC–Co, the compressive intrinsic stress lead to a decrease of tensile residual stress parallel to the surface compared to DCMS-600.

It is not entirely clear, why the thermal and intrinsic residual stress was not detectable for $(Cr,Al)_2C$ in as-deposited coatings. On the measurement side, influences like grain statistics and detector resolution are sufficient for the observation of the stress state. Therefore the reason has to be related to the coating. Without the CTE of the amorphous and $(Cr,Al)_2C$ phase, an in-depth discussion of the stress state in the two phases in the as-deposited state is not possible. However, on basis of the annealing post-treatment results, possible reasons for the absence of residual stress effects are discussed.$(Cr,Al)_2C$ as a metastable phase with distortions as the result of randomly distributed Al and Cr on the Cr-sites and small grain size (see Section 3.2.1) may "shadow" residual stress. However, while this may be possible for intrinsic stress with a lower effect on the Q-value, thermal residual stress should be detectable. The Q difference of dis.-Cr_2AlC (103) reflection between DCMS-600 on WC–Co and HPPMS-600 on IN718 at 100 °C is approx. 0.3 nm^{-1} in 180° azimuth (see Fig. 6e and Fig. 6f). Therefore, a difference in the Q-values for $(Cr,Al)_2C$ in the as-deposited state, resulting from arising σ_{th} during cooling from deposition temperature, should be determinable for the resolution limit of about 0.03 nm^{-1} and 0.05 nm^{-1} for P03 and P07 experiments, respectively.

Since the formation of $(Cr,Al)_2C$ is limited to certain locations on the substrate or interdiffusion barrier surface, mostly amorphous matter is connected to this surface (Section 3.1.1). During cooling from deposition temperature, the amorphous volume act as a buffer for the arising thermal stress and the $(Cr,Al)_2C$ phase remains mostly unaffected from this thermal stress because of the small contact area to the substrate. However, likely, the $(Cr,Al)_2C$ volume

near the coating or interdiffusion barrier is affected by thermal stress. Nevertheless, no evidence in the analysis of P03 and P07 measurements was found.

Distinct extrinsic stress as the result of a volume expansion due to the phase formation is not likely. As the comparison of the (103) curves at 700 °C after first heating in Fig. 6e and Fig. 6f confirms, despite the similar phase is present, the azimuth dependence of Q is only visible for HPPMS-600. Extrinsic stress should be visible for both coatings during phase formation. Additionally amorphous to crystalline transformation is usually associated with volume shrinkage resulting in tensile stress, which can not be seen for HPPMS-600 (Fig. 6e), and is usually not direction-dependent.

3.4. Influence of the deposition process on the mechanical properties

Table 7 summarizes the results of the nanoindentation measurements for the HPPMS-600, HPPMS-600/-70 V, HPPMS-700, and DCMS-600 coatings on IN718 and WC–Co. The results for the Rubalit®708HP substrate showed strong measurement location dependence as the result of the pronounced columnar microstructure in combination with higher roughness and were thereby not considered further.

Considering the error of the hardness values, the hardness of the DCMS and HPPMS coatings is in a similar range of 12 to 14 GPa. HPPMS-600 shows for both substrates the lowest hardness compared to the other HPPMS coatings. The higher hardness of HPPMS-700 on both substrates and HPPMS-600/-70 V on WC–Co may result from the higher amount of crystalline $(Cr,Al)_2C$ compared to HPPMS-600. Because of randomly scattered crystalline $(Cr,Al)_2C$ volumes over the surface and a fixed indent pattern for the measurement, the average hardness for HPPMS-600 corresponds mostly to the amorphous phase. In comparison, as Fig. 2c shows, the HPPMS-700 coating has a high amount of $(Cr,Al)_2C$ near the surface and for higher depth. This may indicate a slightly higher hardness of the crystalline areas compared to the amorphous phase. The origin of the different coating hardness between the two substrates for HPPMS-600/-70 V and DCMS-600 could not be clarified. Influences of the amorphous phase at different depths near the surface (see Fig. 2b) in the case of HPPMS-600/-70 or the broader microstructure for DCMS-600 is possible, but could not be proven. The nanoindentation measurements did not show distinct substrate influences as Fig. 7 proves. A substrate influence on the measurement would lead to a noticeable hardness and Young's modulus increase with increasing depth in the case of WC–Co (H = 15 GPa [64], E = 593 GPa [65]) and a decrease in values for IN718 (H = 4.6 GPa, E = 200 GPa [27]), because of the difference in hardness and Young's modulus to the coating. In the case of DCMS-600, it is possible that the broader microstructure and thereby a higher number of indents near column boundaries decrease the hardness for the coating on WC–Co. The slightly decreased hardness of the DCMS-600 coatings compared to HPPMS-700 may result from the denser microstructure, as discussed in Section 3.1.

The tendencies of Young's modulus values for the different coatings, summarized in Table 7b, follow the differences in hardness and the given explanations apply for the Young's modules as well. The highest Young's modulus was determined for the HPPMS-700 coating with 279 ± 19 GPa and the lowest for HPPMS-600/-70 V with 228 ± 27 GPa and HPPMS-600 with 235 ± 31.

The values in this work are in the range of 245 GPa - 363 GPa for Young's moduli reported in the literature for Cr_2AlC bulk material and thin coatings [4,14,23]. The Young's modulus values determined by Rueß et al. [23] for DCMS and HPPMS coatings with comparable bias voltage are up to 100 GPa higher than the values determined in this work. However, the coatings investigated by Rueß et al.[23] were fully crystallized with varying metastable Cr_2AlC to Cr_2AlC ratios. As described in this section, the deposition process and the resulting properties are complex with a vast amount of influences and therefore those differences are not unlikely. Additionally, as described in [66], several influences on the nanoindentation testing, as the used force of 8 mN in [23] in comparison to 35 mN - 200 mN in this work and a corresponding indentation size effect, can also contribute to the different values.

4. Conclusion

This paper is dedicated to the investigation of the influence of the deposition process, deposition parameters, and substrate on the phase composition, microstructure, residual stress state, and mechanical properties of the Cr-Al-C coating's as-deposited state. Cr-Al-C coatings were deposited by the HPPMS and DCMS processes, with variation of bias voltage and deposition temperature on IN718, WC–Co, and Rubalit®708HP substrates. In-situ heat treatment synchrotron experiments and ex-situ synchrotron experiments were used to determine phase composition and residual stress state in combination with electron microscopy for microstructure and elemental composition investigations. Nanoindentation testing was used for mechanical characterization of the different coating-substrate combinations.

The Cr-Al-C coatings consisted of a metastable crystalline $(Cr,Al)_2C$ and an amorphous phase. A pronounced dependency on the deposition process, leading to the highest crystalline amount for the DCMS coatings with low bias and the lowest crystalline amount for HPPMS coatings with high bias, was observed. Both, increasing deposition temperature and decreasing bias voltage increased the crystalline to amorphous ratio. The microstructure of the $(Cr,Al)_2C$ areas ranged from broader columnar grains with pronounced column boundaries for DCMS coatings to a fine and dense microstructure for the HPPMS coatings. The effect of the deposition process and parameters was highly reduced for the

Table 7
a) Indentation hardness H and b) Indentation Young's modulus E with statistical errors for HPPMS-600, HPPMS-600/-70 V, HPPMS-700, and DCMS-600 coatings on IN718 and WC–Co in the as-deposited state obtained by nanoindentation on the surface.

(a)

	HPPMS-600 H in GPa	HPPMS-600/-70 V H in GPa	HPPMS-700 H in GPa	DCMS-600 H in GPa
IN718	12.1 ± 0.3	12.2 ± 0.4	14.4 ± 0.8	13.2 ± 0.2
WC–Co	12.3 ± 0.7	14.2 ± 0.6	14.1 ± 0.1	11.6 ± 0.6

(b)

	HPPMS-600 E in GPa	HPPMS-600/-70 V E in GPa	HPPMS-700 E in GPa	DCMS-600 E in GPa
IN718	235 ± 31	228 ± 27	279 ± 19	254 ± 14
WC–Co	238 ± 15	271 ± 9	267 ± 6	236 ± 8

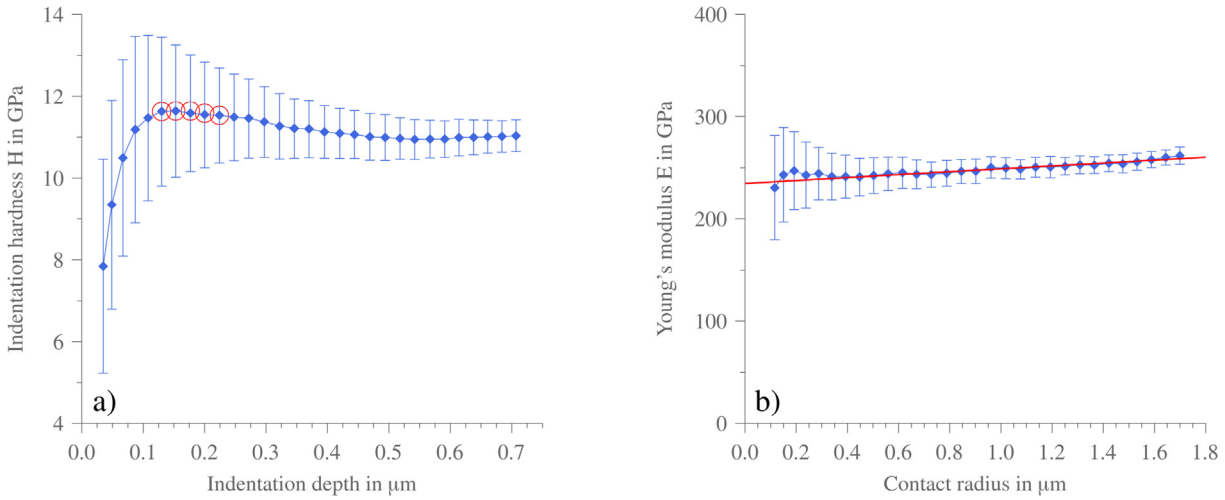

Fig. 7. Exemplary hardness and Young's modulus profiles from the nanoindentation measurements for the DCMS-600 coating on WC–Co substrate. Depth dependence of the a) hardness and b) Young's modulus with marks for the analysis range for hardness and linear fit for the Young's modulus determination.

Rubalit®708HP substrate with high electrical resistivity, resulting in very similar coatings.

The chemical composition of the coatings showed the dependency on the coating process. The Cr/Al ratio was increased for the HPPMS coatings and the amorphous areas as a result of the preferred Al self- and resputtering.

The residual stress investigations revealed the following main results for the Cr-Al-C coating's as-deposited state.

- No evidence for residual stress in the crystalline phase in the DCMS and HPPMS coatings was found.
- Results from a post-heat treatment revealed that the amorphous phase acts as a residual stress buffer.
- The HPPMS process induces higher compressive residual stress than the DCMS process.
- The compressive intrinsic stress reduces tensile residual stress during cooling for coatings on WC–Co and increases resulting compressive residual stress for IN718 substrate.
- The intrinsic residual stress from the ion bombardment is mainly planar and parallel to the surface, while thermal stress is 3-dimensional for the coating thickness of approx. 5 µm.
- The compressive residual stress is not stable at temperatures of 700 °C and above.

The Cr-Al-C coatings exhibited hardness values in the range of 11.6 ±0.6 GPa to 14.4 ±0.8 GPa and Young's modulus values in the range of 228 ±27 GPa to 279 GPa ±19 GPa. A decrease in both, hardness and youngs modulus was observed for the DCMS coatings.

5. Data availability

The raw data required to reproduce these findings cannot be shared at this time as the data also forms part of an ongoing study. The processed data required to reproduce these findings cannot be shared at this time as the data also forms part of an ongoing study.

Declaration of Competing Interest

The authors declare that they have no known competing financial interests or personal relationships that could have appeared to influence the work reported in this paper.

Acknowledgements

Max Thorhauer and Dr. Axel Marquardt are thanked for their great help and time during the experiments at DESY. Julius Hendl is acknowledged for the helpful proofreading and discussions.

Funding: This work was supported by the Deutsche Forschungsgemeinschaft (DFG) [Grant No. LE1373/41–1]; and Deutsche Elektronen und Synchrotron (DESY) [proposals I-20170652 and I-20180296].

References

[1] M.W. Barsoum, The MN+1AXN phases: A new class of solids: Thermodynamically stable nanolaminates, Prog. Solid State Chem. 28 (1–4) (2000) 201–281, https://doi.org/10.1016/S0079-6786(00)00006-6.
[2] M.W. Barsoum, M. Radovic, Elastic and mechanical properties of the MAX phases, Annu. Rev. Mater. Res. 41 (1) (2011) 195–227, https://doi.org/10.1146/annurev-matsci-062910-100448.
[3] W. Tian, P. Wang, G. Zhang, Y. Kan, Y. Li, D. Yan, Synthesis and thermal and electrical properties of bulk Cr2AlC, Scripta Mater. 54 (5) (2006) 841–846, https://doi.org/10.1016/j.scriptamat.2005.11.009.
[4] J.D. Hettinger, S.E. Lofland, P. Finkel, T. Meehan, J. Palma, K. Harrell, S. Gupta, A. Ganguly, T. El-Raghy, M.W. Barsoum, Electrical transport, thermal transport, and elastic properties of M2AlC (M = Ti, Cr, Nb, and V), Phys. Rev. B 72 (11) (2005), https://doi.org/10.1103/PhysRevB.72.115120.
[5] D.J. Tallman, B. Anasori, M.W. Barsoum, A critical review of the oxidation of Ti2AlC, Ti3AlC2 and Cr2AlC in air, Mater. Res. Lett. 1 (3) (2013) 115–125, https://doi.org/10.1080/21663831.2013.806364.
[6] J.L. Smialek, Oxidation of Al2O3 scale-forming MAX phases in turbine environments, Metall. Mater. Trans. A (2017), https://doi.org/10.1007/s11661-017-4346-9.
[7] Z.J. Lin, M.S. Li, J.Y. Wang, Y.C. Zhou, High-temperature oxidation and hot corrosion of Cr2AlC, Acta Mater. 55 (18) (2007) 6182–6191, https://doi.org/10.1016/j.actamat.2007.07.024.
[8] J. Ward, D. Bowden, E. Prestat, S. Holdsworth, D. Stewart, M.W. Barsoum, M. Preuss, P. Frankel, Corrosion performance of Ti3SiC2, Ti3AlC2, Ti2AlC and Cr2AlC MAX phases in simulated primary water conditions, Corros. Sci. 139 (2018) 444–453, https://doi.org/10.1016/j.corsci.2018.04.034.
[9] M. Ougier, A. Michau, F. Schuster, H. Maskrot, M.L. Schlegel, Effects of HiPIMS discharges and annealing on Cr-Al-C thin films, Surf. Coat. Technol. 399 (2020) 126141, https://doi.org/10.1016/j.surfcoat.2020.126141.
[10] R. Mertens, Z. Sun, D. Music, J. Schneider, Effect of the composition on the structure of Cr-Al-C investigated by combinatorial thin film synthesis and ab initio calculations, Adv. Eng. Mater. 6 (11) (2004) 903–907, https://doi.org/10.1002/adem.200400096.
[11] Q.M. Wang, A. Flores Renteria, O. Schroeter, R. Mykhaylonka, C. Leyens, W. Garkas, M. to Baben, Fabrication and oxidation behavior of Cr2AlC coating on Ti6242 alloy, Surf. Coat. Technol. 204 (15) (2010) 2343–2352, https://doi.org/10.1016/j.surfcoat.2010.01.002.
[12] J.M. Schneider, Z. Sun, R. Mertens, F. Uestel, R. Ahuja, Ab initio calculations and experimental determination of the structure of Cr2AlC, Solid State Commun. 130 (7) (2004) 445–449, https://doi.org/10.1016/j.ssc.2004.02.047.

[13] C. Walter, D.P. Sigumonrong, T. El-Raghy, J.M. Schneider, Towards large area deposition of Cr2AlC on steel, Thin Solid Films 515 (2) (2006) 389–393, https://doi.org/10.1016/j.tsf.2005.12.219.
[14] J.M. Schneider, D.P. Sigumonrong, D. Music, C. Walter, J. Emmerlich, R. Iskandar, J. Mayer, Elastic properties of Cr2AlC thin films probed by nanoindentation and ab initio molecular dynamics, Scripta Mater. 57 (12) (2007) 1137–1140, https://doi.org/10.1016/j.scriptamat.2007.08.006.
[15] J.J. Li, Y.H. Qian, D. Niu, M.M. Zhang, Z.M. Liu, M.S. Li, Phase formation and microstructure evolution of arc ion deposited Cr2AlC coating after heat treatment, Appl. Surf. Sci. 263 (2012) 457–464, https://doi.org/10.1016/j.apsusc.2012.09.082.
[16] E.I. Zamulaeva, E.A. Levashov, T.A. Sviridova, N.V. Shvyndina, M.I. Petrzhik, Pulsed electrospark deposition of MAX phase Cr2AlC based coatings on titanium alloy, Surf. Coat. Technol. 235 (2013) 454–460, https://doi.org/10.1016/j.surfcoat.2013.08.002.
[17] C. Tang, M. Steinbrück, M. Klimenkov, U. Jäntsch, H.J. Seifert, S. Ulrich, M. Stüber, Textured growth of polycrystalline MAX phase carbide coatings via thermal annealing of M/C/Al multilayers, J. Vacuum Sci. Technol. A 38 (1) (2019) 013401, https://doi.org/10.1116/1.5131544.
[18] K. Sarakinos, J. Alami, S. Konstantinidis, High power pulsed magnetron sputtering: A review on scientific and engineering state of the art, Surf. Coat. Technol. 204 (11) (2010) 1661–1684, https://doi.org/10.1016/j.surfcoat.2009.11.013.
[19] D. Shtansky, P. Kiryukhantsev-Korneev, A. Sheveyko, B. Mavrin, C. Rojas, A. Fernandez, E. Levashov, Comparative investigation of TiAlC(N), TiCrAlC(N), and CrAlC(N) coatings deposited by sputtering of MAX-phase Ti2-xCrxAlC targets, Surf. Coat. Technol. 203 (23) (2009) 3595–3609, https://doi.org/10.1016/j.surfcoat.2009.05.036.
[20] H. Rueß, M. to Baben, S. Mráz, L. Shang, P. Polcik, S. Kolozsvári, M. Hans, D. Primetzhofer, J. Schneider, HPPMS deposition from composite targets: Effect of two orders of magnitude target power density changes on the composition of sputtered Cr-Al-C thin films, Vacuum 145 (2017) 285–289. doi:10.1016/j.vacuum.2017.08.048.
[21] S.M. Schmuecker, D. Clouser, T.J. Kraus, B.M. Leonard, Synthesis of metastable chromium carbide nanomaterials and their electrocatalytic activity for the hydrogen evolution reaction, Dalton Trans. 46 (39) (2017) 13524–13530, https://doi.org/10.1039/C7DT01404J.
[22] A. Abdulkadhim, M. to Baben, T. Takahashi, V. Schnabel, M. Hans, C. Polzer, P. Polcik, J.M. Schneider, Crystallization kinetics of amorphous Cr2AlC thin films, Surface and Coatings Technology 206 (4) (2011) 599–603. doi:10.1016/j.surfcoat.2011.06.003.
[23] H. Rueß, J. Werner, Y. Unutulmazsoy, J.W. Gerlach, X. Chen, B. Stelzer, D. Music, S. Kolozsvari, P. Polcik, T.E. Weirich, J.M. Schneider, Effect of target peak power density on the phase formation, microstructure evolution, and mechanical properties of Cr2AlC MAX-phase coatings, J. Eur. Ceram. Soc. 41 (3) (2021) 1841–1847, https://doi.org/10.1016/j.jeurceramsoc.2020.10.072.
[24] P. Eklund, M. Beckers, U. Jansson, H. Högberg, L. Hultman, The Mn+1AXn phases: Materials science and thin-film processing, Thin Solid Films 518 (8) (2010) 1851–1878, https://doi.org/10.1016/j.tsf.2009.07.184.
[25] M. Ougier, A. Michau, F. Lomello, F. Schuster, H. Maskrot, M.L. Schlegel, High-temperature oxidation behavior of HiPIMS as-deposited Cr–Al–C and annealed Cr2AlC coatings on Zr-based alloy, J. Nucl. Mater. 528 (2020) 151855, https://doi.org/10.1016/j.jnucmat.2019.151855.
[26] S. Heinze, A. Stark, J. Hendl, C. Leyens, Influence of the deposition process on the Cr2AlC phase formation during heat treatment of Cr-Al-C thin films, SSRN Electron. J. (2022), https://doi.org/10.2139/ssrn.4168644.
[27] HAYNES 718 alloy brochure, http://haynesintl.com/docs/default-source/pdfs/new-alloy-brochures/high-temperature-alloys/brochures/718-brochure.pdf?sfvrsn=14, (accessed 15 June 2022) (2022).
[28] CeramTec, Rubalit 708 HP - Data Sheet, https://www.ceramtec.com/files/el_keramische_sinterunterlagen_de.pdf, (accessed 15 June 2022) (2022).
[29] M.V. Frandsen, W.S. Williams, Thermal conductivity and electrical resistivity of cemented transition-metal carbides at low temperatures, J. Am. Ceram. Soc. 74 (6) (1991) 1411–1416, https://doi.org/10.1111/j.1151-2916.1991.tb04121.x.
[30] H. Wang, T. Webb, J.W. Bitler, Study of thermal expansion and thermal conductivity of cemented WC–Co composite, Int. J. Refract. Met. Hard Mater. 49 (2015) 170–177, https://doi.org/10.1016/j.ijrmhm.2014.06.009.
[31] S.-S. Park, S.-G. Yoon, High Temperature Oxidation of TiAlN Thin Films for Memory Devices, Integr. Ferroelectr. 48 (1) (2002) 281–290, https://doi.org/10.1080/713718323.
[32] R. Rachbauer, S. Massl, E. Stergar, D. Holec, D. Kiener, J. Keckes, J. Patscheider, M. Stiefel, H. Leitner, P.H. Mayrhofer, Decomposition pathways in age hardening of Ti-Al-N films, J. Appl. Phys. 110 (2) (2011) 023515, https://doi.org/10.1063/1.3610451.
[33] M. Bartosik, D. Holec, D. Apel, M. Klaus, C. Genzel, J. Keckes, M. Arndt, P. Polcik, C.M. Koller, P.H. Mayrhofer, Thermal expansion of Ti-Al-N and Cr-Al-N coatings, Scripta Mater. 127 (2017) 182–185, https://doi.org/10.1016/j.scriptamat.2016.09.022.
[34] C. Krywka, J. Keckes, S. Storm, A. Buffet, S.V. Roth, R. Döhrmann, M. Müller, Nanodiffraction at MINAXS (P03) beamline of PETRA III, J. Phys: Conf. Ser. 425 (7) (2013) 072021, https://doi.org/10.1088/1742-6596/425/7/072021.
[35] N. Schell, A. King, F. Beckmann, T. Fischer, M. Müller, A. Schreyer, The high energy materials science beamline (HEMS) at PETRA III, Mater. Sci. Forum 772 (2013) 57–61, https://doi.org/10.4028/www.scientific.net/MSF.772.57.
[36] A.P. Hammersley, FIT2D: An introduction and overview ESRF97HA02T (1997). Tech. Rep..
[37] A.P. Hammersley, S.O. Svensson, M. Hanfland, A.N. Fitch, D. Hausermann, Two-dimensional detector software: From real detector to idealised image or two-theta scan, High Press. Res. 14 (4–6) (1996) 235–248, https://doi.org/10.1080/08957959608201408.
[38] Match! - Phase Analysis using Powder Diffraction, Dr. H. Putz & Dr. K. Brandenburg GbR.
[39] Cr2AlC crystal structure: Datasheet from "PAULING FILE multinaries edition – 2012" in SpringerMaterials, (accessed 15 June 2022) (2016).
[40] Cr7C3 crystal structure: Datasheet from "PAULING FILE multinaries edition – 2012" in SpringerMaterials, (accessed 15 June 2022) (2016).
[41] Mo2C (MoC0.5 ht2) crystal structure: Datasheet from "PAULING FILE multinaries edition – 2012" in SpringerMaterials, (accessed 15 June 2022) (2016).
[42] S. Gražulis, D. Chateigner, R.T. Downs, A.F.T. Yokochi, M. Quirós, L. Lutterotti, E. Manakova, J. Butkus, P. Moeck, A. Le Bail, Crystallography Open Database – an open-access collection of crystal structures, J. Appl. Crystallogr. 42 (4) (2009) 726–729, https://doi.org/10.1107/S0021889809016690.
[43] T. Chudoba, Dynamikmodul, https://www.asmec.de/en/product.php?seite=0&useite=8, (accessed 15 June 2022) (Mar. 2022).
[44] W. Oliver, G. Pharr, An improved technique for determining hardness and elastic modulus using load and displacement sensing indentation experiments, J. Mater. Res. 7 (6) (1992) 1564–1583, https://doi.org/10.1557/JMR.1992.1564.
[45] D.E. Newbury, D.C. Joy, P. Echlin, C.E. Fiori, J.I. Goldstein, Electron Channeling Contrast in the SEM, Springer US, Boston, MA, 1986, pp. 87–145. doi:10.1007/978-1-4757-9027-6_3.
[46] G. Greczynski, J. Lu, J. Jensen, I. Petrov, J.E. Greene, S. Bolz, W. Kölker, C. Schiffers, O. Lemmer, L. Hultman, Metal versus rare-gas ion irradiation during Ti1-xAlxN film growth by hybrid high power pulsed magnetron/dc magnetron co-sputtering using synchronized pulsed substrate bias, J. Vacuum Sci. Technol. A 30 (6) (2012) 061504, https://doi.org/10.1116/1.4750485.
[47] S. Mráz, J. Emmerlich, F. Weyand, J.M. Schneider, Angle-resolved evolution of the composition of Cr–Al–C thin films deposited by sputtering of a compound target, J. Phys. D: Appl. Phys. 46 (13) (2013) 135501, https://doi.org/10.1088/0022-3727/46/13/135501.
[48] S. Berg, I.V. Katardjiev, Preferential sputtering effects in thin film processing, J. Vacuum Sci. Technol. A: Vacuum, Surf., Films 17 (4) (1999) 1916–1925, https://doi.org/10.1116/1.581704.
[49] I. Arganda-Carreras, V. Kaynig, C. Rueden, K.W. Eliceiri, J. Schindelin, A. Cardona, H. Sebastian Seung, Trainable Weka Segmentation: A machine learning tool for microscopy pixel classification, Bioinformatics 33 (15) (2017) 2424–2426, https://doi.org/10.1093/bioinformatics/btx180.
[50] J. Schindelin, I. Arganda-Carreras, E. Frise, V. Kaynig, M. Longair, T. Pietzsch, S. Preibisch, C. Rueden, S. Saalfeld, B. Schmid, J.-Y. Tinevez, D.J. White, V. Hartenstein, K. Eliceiri, P. Tomancak, A. Cardona, Fiji: An open-source platform for biological-image analysis, Nat. Methods 9 (7) (2012) 676–682, https://doi.org/10.1038/nmeth.2019.
[51] B.-Q. Fu, W. Liu, Z.-L. Li, Calculation of the surface energy of hcp-metals with the empirical electron theory, Appl. Surf. Sci. 255 (23) (2009) 9348–9357, https://doi.org/10.1016/j.apsusc.2009.07.034.
[52] U.F. Kocks, H.-R. Wenk, A.J. Beaudoin, H. Mecking, C.N. Tomé, C.N. Tomé (Eds.), Texture and Anisotropy: Preferred Orientations in Polycrystals and Their Effect on Materials Properties, first paperback edition (with corrections) Edition, Cambridge University Press, Cambridge, 2000.
[53] Y. Wang, J. Huang, Texture analysis in hexagonal materials, Mater. Chem. Phys. 81 (1) (2003) 11–26, https://doi.org/10.1016/S0254-0584(03)00168-8.
[54] E. Macherauch, Neuere Untersuchungen zur Ausbildung und Auswirkung von Eigenspannungen in metallischen Werkstoffen, Materialwiss. Werkstofftech. 10 (3) (1979) 97–111, https://doi.org/10.1002/mawe.19790100309.
[55] R. Daniel, D. Holec, M. Bartosik, J. Keckes, C. Mitterer, Size effect of thermal expansion and thermal/intrinsic stresses in nanostructured thin films: Experiment and model, Acta Mater. 59 (17) (2011) 6631–6645, https://doi.org/10.1016/j.actamat.2011.07.018.
[56] J.A. Thornton, D. Hoffman, Stress-related effects in thin films, Thin Solid Films 171 (1) (1989) 5–31, https://doi.org/10.1016/0040-6090(89)90030-8.
[57] D. Magnfält, G. Abadias, K. Sarakinos, Atom insertion into grain boundaries and stress generation in physically vapor deposited films, Appl. Phys. Lett. 103 (5) (2013) 051910, https://doi.org/10.1063/1.4817669.
[58] R. Daniel, J. Keckes, I. Matko, M. Burghammer, C. Mitterer, Origins of microstructure and stress gradients in nanocrystalline thin films: The role of growth parameters and self-organization, Acta Mater. 61 (16) (2013) 6255–6266, https://doi.org/10.1016/j.actamat.2013.07.009.
[59] I. Petrov, P.B. Barna, L. Hultman, J.E. Greene, Microstructural evolution during film growth, J. Vacuum Sci. Technol. A: Vacuum, Surf., Films 21 (5) (2003) S117–S128, https://doi.org/10.1116/1.1601610.
[60] C. Davis, A simple model for the formation of compressive stress in thin films by ion bombardment, Thin Solid Films 226 (1) (1993) 30–34, https://doi.org/10.1016/0040-6090(93)90201-Y.
[61] Y. Pauleau, Generation and evolution of residual stresses in physical vapour-deposited thin films, Vacuum 61 (2–4) (2001) 175–181, https://doi.org/10.1016/S0042-207X(00)00475-9.

[62] R. Daniel, K. Martinschitz, J. Keckes, C. Mitterer, The origin of stresses in magnetron-sputtered thin films with zone T structures, Acta Mater. 58 (7) (2010) 2621–2633, https://doi.org/10.1016/j.actamat.2009.12.048.
[63] H. Hu, X. Chen, X. Zhao, N. Li, Ab initio molecular dynamics study on thermal expansion of solid-solution compounds in MAX phase, Comput. Mater. Sci. 103 (2015) 200–203, https://doi.org/10.1016/j.commatsci.2015.03.034.
[64] R.W. Armstrong, The hardness and strength properties of WC-Co composites, Materials 4 (7) (2011) 1287–1308, https://doi.org/10.3390/ma4071287.
[65] H. Doi, Y. Fujiwara, K. Miyake, Y. Oosawa, A systematic investigation of elastic moduli of Wc-Co alloys, Metall. Mater. Trans. B 1 (5) (1970) 1417–1425, https://doi.org/10.1007/BF02900264.
[66] G.M. Pharr, E.G. Herbert, Y. Gao, The indentation size effect: A critical examination of experimental observations and mechanistic interpretations, Annu. Rev. Mater. Res. 40 (1) (2010) 271–292, https://doi.org/10.1146/annurev-matsci-070909-104456.